

# Computation of hydrogen-air mixture detonation with OpenMP multiprocessing on a supercomputer

Nikitin V.F., Smirnov N.N., Stamov L.I., Altoukhov D.I.  
mech.math.msu@inbox.ru

## Abstract

The aim of the present study is to calculate the process of detonation combustion of hydrogen-air gas mixtures in engines. Development and verification of 3-d transient mathematical model of chemically reacting gas mixture flows incorporating hydrogen was performed. Development of a computational model based on the mathematical one for parallel computing on supercomputers incorporating CPU and GPU units was carried out. Investigation of the influence of computational grid size on simulation precision and computational speed was performed. Investigation of calculation runtime acceleration was carried out subject to variable number of parallel threads on different architectures and implying different strategies of parallel computation.

## Introduction

Hydrogen is a very perspective fuel making the engine exhaust much cleaner than that for hydrocarbon combustion. The advantages of a constant volume combustion cycle as compared to constant pressure combustion in terms of thermodynamic efficiency has focused the search for advanced propulsion on detonation engines. The thermodynamic efficiency of Chapman-Jouguet detonation as compared with slow combustion modes is due to the minimal entropy of the exhaust jet. During the past several decades different schemes of pulse detonation engines were suggested aimed to demonstrate that proper utilization of the operation cycle does result in improved performance. There still exist many issues in developing this technology, which represent scientific and technological challenges. In particular, it is not clear up to now, which principle of pulse detonating cycle is more effective: co-flow or counter-flow detonation wave propagation, what cycle is preferable: pulse detonation or rotating detonation. The success in resolving these problems will determine the implementation of detonation propulsion. Extensive numerical multidimensional simulations of detonation onset and propagation are necessary in combustion chambers able to distinguish optimal scheme for the operation cycle. Parallel computing is a powerful tool enabling to make simulations more effective and less time consuming. However not all numerical problems allow effective parallelization. The aim of the present study is developing effective mathematical model and numerical scheme for unsteady detonations simulation and investigating its parallelization potential for supercomputing

# 1 Mathematical model

## Equations

In order to calculate multicomponent gas dynamics with chemical reactions excluding transport phenomena effects and considering external mass and energy sources we use the following set of simultaneous equations:

$$\frac{\partial \rho_k}{\partial t} + \frac{\partial(\rho_k u_j)}{\partial x_j} = \dot{\omega}_k + \dot{M}_k \quad (1.1a)$$

$$\frac{\partial \rho u_i}{\partial t} + \frac{\partial(\rho u_i u_j)}{\partial x_j} + \frac{\partial p}{\partial x_j} = 0 \quad (1.1b)$$

$$\frac{\partial(E + \rho \frac{u^2}{2})}{\partial t} + \frac{\partial(E + p + \rho \frac{u^2}{2})}{\partial x_j} = \dot{Q} + \dot{Q}_M \quad (1.1c)$$

In equations 1.1 index  $k$  takes values  $1..N_c$  (number of components) and indices  $i, j$  - values 1, 2, 3 (number of dimensions); repeated indices presume summation. In total there is  $N_c + 4$  differential equations in the set.

## Algebraic relations.

Differential equations 1.1 are to be complemented with three algebraic relations and algebraic representations for chemical and mass and energy sources. First three relations will look like:

$$\rho = \sum_{k=1}^{N_c} \rho_k, p = R_G T \sum_{k=1}^{N_c} \frac{\rho_k}{W_k}, E = R_G T \sum_{k=1}^{N_c} \frac{\rho_k}{W_k} (\hat{H}_k(T) - 1) \quad (1.2)$$

Relations 1.2 define gas density  $\rho$ , pressure  $p$  and internal energy per unit volume  $E$  of mixture respectively. Other definitions are:  $R_G$  -universal gas constant,  $W_k$  molar weight of a component, and for temperature functions  $\hat{H}_k(T)$  dimensionless enthalpy of a component encompassing enthalpy of formation at given temperature  $T_{ref}$  (chemical energy). More precisely the conception of dimensionless thermodynamic data is given in [1]. As these expressions show, in algebraic expressions here and in what follows it is often convenient to use molar density  $X_k$  (which sometimes, especially in chemical literature, is called "concentration") instead of partial component density  $\rho_k$ :

$$X_k = \frac{\rho_k}{W_k} \quad (1.3)$$

Mass source  $\dot{\omega}_k$  is due to chemical interactions present in the system of gases. Mass source  $\dot{M}_k$  results from the external source outcome. Source  $\dot{Q}_M$  in energy equation is a total income of energy carried with the external mass  $\dot{M}_k$ ; source  $\dot{Q}$

in energy equation denotes extra energy income from the external source. Thermal energy source implying chemical reactions inside the system is absent in this model because energy  $E$  already encompasses chemical energy of each component. External sources are not directly linked with chemical interactions inside the system; they aim to inject mass and energy in gas mixture from the outside for ignition and movement excitation. In our problem setup they explicitly depend on time and location. Chemical sources  $\dot{\omega}_k$  for most systems take a complicated form; they can be expressed depending on temperature  $T$  and set of the molar densities  $X = \{X_k\}$ ; sum of these sources equals zero due to the law of mass conservation in chemical reactions:

$$\dot{\omega}_k = W_k \hat{\omega}_k(T, X), \sum_{k=1}^{N_c} \dot{\omega}_k = 0 \quad (1.4)$$

There also exist more precise laws of chemical interactions (law of mass conservation for each element), which are taken into account in kinetic mechanism and can be considered in numerical realization of the model for calculation simplification and precision improvement. General form of chemical sources is quite complicated and includes members which are nonlinear for each argument; the common view is

$$\omega_r = M_r(X) \left[ k_{F,r}(M_r, T) \prod_j X_j^{\alpha_{r,j}} - k_{B,r}(M_r, T) \prod_j X_j^{\beta_{r,j}} \right] \quad (1.5)$$

where  $\omega_r$  is speed (intensity) of reaction  $r$ ,  $\nu_{r,k}$  is an algebraic stoichiometric coefficient of a component  $k$  in reaction  $r$ ,  $M_r$  is a third bodies influence coefficient (those which don't change) in the reaction  $r$ , which equals 1 when this influence is absent,  $k_{F,r}$  is a speed coefficient of a forward reaction, usually depending solely on temperature, but for some (out-of-order) reactions also of  $M_r$ ,  $k_{B,r}$  is a speed coefficient of the backward reaction,  $\alpha_{r,j}$  are powers of components in the forward reaction (usually, but not always nonzero only for incoming components)  $\beta_{r,j}$  powers of components in the backward reaction.

Dependencies  $\hat{A}_k(T)$  are often expressed as polynomials with different coefficients for different components. Those components calculation based on the tabular data on heat capacity at different temperatures and data on the enthalpy of formation is a subject for thermodynamic modeling of gas mixture. We took our data from the source [2]; these data format is described in detail in manuals [1] and [3].

## Transformation of equations for the component mass

In practice equation 1.1 can be used both per se and transformed to the following view:

$$\frac{\partial \rho}{\partial t} + \frac{\partial(\rho u_j)}{\partial x_j} = \dot{M} = \sum_k \dot{M}_k \quad (1.6a)$$

$$\frac{\partial Y_k}{\partial t} + u_j \frac{\partial Y_k}{\partial x_j} = \frac{\dot{\omega}_k + \dot{M}_k}{\rho} = S_k \quad (1.6b)$$

Where  $Y_k$  stands for mass concentration of a component:

$$Y_k = \frac{\rho_k}{\rho} = \frac{\rho_k}{\sum_j \rho_j} = \frac{X_k W_k}{\sum_j X_j W_j} \quad (1.7)$$

Transformation of equation 1.1 into set 1.6 results into that the whole set has now more equations than algebraically independent variables. There are following solutions for this situations:

- Substitute one of equations 1.6b (on choice with number  $m$ ) with an algebraic relation following the definition 1.7:

$$Y_m = 1 - \sum_{k \neq m} Y_k \quad (1.8)$$

- Make calculations on each timestep of the overdetermined set as if variables  $Y_k$  were independent. After each timestep to carry out correction delivering satisfaction of conditions (1.10) in a way different from (1.11). Let  $Y_k$  be values of mass concentrations before correction and  $\tilde{Y}_k$  - after. Correction that retains proportions and preserves from sign change look like:

$$\tilde{Y}_k = \frac{Y_k}{\sum_j Y_j} \quad (1.9)$$

- On each timestep perform calculation over overdetermined set as the variables  $Y_k$  were independent, but without any correction, at least on each step. Instead value of this imbalance

$$\epsilon_Y = \left| 1 - \sum_k Y_k \right| \quad (1.10)$$

is taken as one of the method accuracy measures. In case this value excesses certain predefined level, it can be decided to perform correction before proceeding calculation or we can judge about method's scope of applicability.

## Sources of mass and energy

Such a problem setup causes mass sources  $\dot{M}_k$  and energy sources  $\dot{Q}_M, \dot{Q}$ , can be expressed as

$$\dot{M}_k = \frac{\Delta M_k}{t_{ign} \Omega_{ign}} \cdot \begin{cases} 1, & |x - x_{ign}| \leq r_{ign}, 0 \leq t \leq t_{ign} \\ 0, & \text{otherwise} \end{cases} \quad (1.11a)$$

$$\dot{Q} = \frac{\Delta Q}{t_{ign} \Omega_{ign}} \cdot \begin{cases} 1, & |x - x_{ign}| \leq r_{ign}, 0 \leq t \leq t_{ign} \\ 0, & \text{otherwise} \end{cases} \quad (1.11b)$$

$$\dot{Q}_M = \sum_k \dot{M}_k e_k(T_q) = R_G T_q \sum_k \dot{M}_k (\hat{H}_k(T_q) - 1) \quad (1.11c)$$

Denotations are:  $\Delta$  is total mass of component  $k$  from the external source,  $\Delta Q$  - total extra energy income from the external source. Energy, coming with mass 1.11c is determined from the condition that before mixing with gas components of the system gas temperature was  $T_q$ . Volume in which energy is released, is a volume of a sphere:

$$\Omega_{\text{ign}} = \frac{4\pi}{3} r_{\text{ign}}^3 \quad (1.12)$$

given that ignition center  $x_{\text{ign}}$  lays inside the working area on a distance of less then  $r_{\text{ign}}$  from the nearest wall (otherwise a necessary correction of this volume should be taken in accordance to formulae having this distance as an argument; present paper doesn't consider this case).

## Boundary conditions

Closed from each side wall in our model corresponds to the impermeability condition on it:

$$\mathbf{u} \cdot \mathbf{n} = 0 \text{ given } \mathbf{x} \in \partial\Omega \quad (1.13)$$

where  $\partial\Omega$  is a boundary of the working area,  $\mathbf{n}$  is a normal vector at a given point (for a condition 1.13 it is irrelevant, which one: internal or external). Condition 1.13 is sufficient, but for numerical realization of the model its and equations 1.1b corollary, which states, that normal to the wall pressure derivative component equals zero, may be needed:

$$\mathbf{n} \cdot \nabla p = 0 \text{ given } \mathbf{x} \in \partial\Omega \quad (1.14)$$

### 1.1 Initial conditions

In order to solve problem 1.1 it is necessary to know the state of all the algebraically independent variables at time  $t = 0$ . Across the whole area at that time temperature  $T_{\text{ini}}$  and pressure  $P_{\text{ini}}$  are set. Initial velocity is assumed to be zero. Initial concentrations of components are given through their nonnormalized molar fractions (which for ideal gases are equivalent to the volume fractions), which we will denote  $C_{\text{ini},k}$ , and by that ratio of molar densities  $[\text{H}_2] : [\text{O}_2] : [\text{N}_2]$  will look like (instead of numbers of components it is convenient to use their chemical formulas as literals). Recalculation to the partial densities and to molar fractions is performed with account of the initial pressure and temperature with formulae (different variants can be used in different realizations)

$$Y_k = \frac{C_k W_k}{\sum_j C_j W_j}, \rho = \frac{P_{\text{ini}}}{R_G T_{\text{ini}} \sum_k Y_k / W_k}, \rho_k = \rho Y_k = \frac{P_{\text{ini}} C_k W_k}{R_G T_{\text{ini}} \sum_k C_j} \quad (1.15)$$

## Chapman-Jouguet detonation and Neumann peak parameters calculation.

Parameters of Chapman-Jouguet detonation and Neumann peak, which, according to ZND-theory (Zeldovich-Neumann-Döring), moves ahead of the chemical reactions zone, are calculated according to the gas dynamics jumps theory making use only of thermodynamics of components of the gas mixture, and without involving any chemical kinetics data; only mere presence of chemical transformations pushing system towards chemical equilibrium is presumed.

We will denote parameters with the upper index 0 as initial, the final ones, after the shock (with possible change in mixture compound) without upper index. With a lower index we will denote numbers of components and (at the equilibrium state calculation) chemical elements.

Detonation wave (strong discontinuity) propagates through the resting media with a speed  $D$  in the positive direction. Mass, momentum and total enthalpy conservation of the media at the strong discontinuity lead to the following conditions in coordinate system bound to the wave:

$$-\rho^0 D = \rho v \quad (1.16a)$$

$$\rho^0 D^2 + p^0 = \rho v^2 + p \quad (1.16b)$$

$$h^0 + \frac{1}{2} D^2 = h + \frac{1}{2} v^2 \quad (1.16c)$$

Pressure and enthalpy algebraically depend on such gas parameters as density  $\rho$ , temperature  $T$  and molar concentrations per unit volume  $N_k$ ,  $1 \leq k \leq N_C$ . Obviously, equations 1.16 don't give an univocal answer about parameters behind the detonation wave without any extra conditions, as mixture compound there doesn't change.

Such an extra condition is one of chemical equilibrium behind the detonation wave. Here we will outline an algorithm capable of finding the speed of detonation wave and parameters behind it (specifically, behind the chemical reactions zone). The algorithm is based on wave speed minimization for a given value of density behind the wave  $\rho$ . The algorithm is set forth in the GALCIT report [4]. It doesn't pretend to find exact conditions behind the detonation wave as well as an exact value of speed the thing here is that chemical equilibrium establishment is assumed to happen at least before the gas mixture behind the detonation wave has met the sonic line i.e. quite rapidly. This holds true for many reactions accompanying combustion but not for all.

### First part of the algorithm: $D(\rho)$ calculation.

1. Input conditions in front of the wave:  $p^0, T^0, N_k^0$ ; determine  $\rho^0$  and  $h^0$ ; input tolerances  $\epsilon_R, \epsilon_A$  and increments  $\Delta_D, \Delta_T$ ; input  $\rho$ .
2. Input initial guess  $D = 2000, T = 2000$

3. Find equilibrium state ( $\mathbf{N}_k$ ) by initial ( $\mathbf{N}_k^0$ ) at given  $T$  under the condition of constant density  $\rho$ .
4. Calculate  $(H, P)(D, T)$

$$v = D \frac{\rho^0}{\rho} \quad (1.17a)$$

$$H = \left( h(T, \mathbf{N}_j) + \frac{v^2}{2} \right) - \left( h^0 + \frac{D^2}{2} \right) \quad (1.17b)$$

$$P = (p(T, \rho, \mathbf{N}_j + \rho v^2) - (p^0 + \rho^0 D^2)) \quad (1.17c)$$

5. Calculate  $(H_T, P_T)(T + \Delta_T, D)$  and  $(H_D, P_D)(T, D + \Delta_D)$ , and then recalculate Jacobi matrix components

$$H_T = \frac{H_T - H}{\Delta_T}, H_D = \frac{H_D - H}{\Delta_D}, P_T = \frac{P_T - P}{\Delta_T}, P_D = \frac{P_D - P}{\Delta_D} \quad (1.18)$$

6. Solve linear 2 x 2 problem (e.g., by Kramer method) subject to corrections  $\delta_T, \delta_D$ :

$$H_T \delta_T + H_D \delta_D = -H, P_T \delta_T + P_D \delta_D = -P \quad (1.19)$$

Solution of (6) looks like:

$$\mathbf{Z} = \begin{vmatrix} H_T & H_D \\ P_T & P_D \end{vmatrix}, \delta_T = -\mathbf{Z}^{-1} \begin{vmatrix} H & H_D \\ P & P_D \end{vmatrix}, \delta_D = -\mathbf{Z}^{-1} \begin{vmatrix} H_T & H \\ P_T & P \end{vmatrix} \quad (1.20)$$

7. Calculate correction  $T = T + \delta_T, D = D + \delta_D$ , . Make sure that convergence criterion is met

$$|\delta_T| < \epsilon_R T + \epsilon_A, |\delta_D| < \epsilon_R D + \epsilon_A \quad (1.21)$$

If criterion 1.21 isn't satisfied, go to step 3.

8. Find equilibrium state ( $\mathbf{N}_k$ ) by the initial ( $\mathbf{N}_k^0$ ) at given  $T$  under the condition of constant density  $\rho$ . Find  $p(T, \rho, \mathbf{N}_j)$  and  $h(T, \mathbf{N}_j)$ . Do this in case the final values behind the detonation are needed. Exit.

## Second part of the algorithm - $D(\rho)$ minimization.

Based on the golden section method (instead of the bulky method described in [4]). This part encompasses the previous algorithm.

1. Input  $X_{\min}(= 1.5)$  and  $X_{\max}(= 2.0)$ , and also initial data in front of the detonation wave and other source data for the algorithm, calculating  $D(\rho)$ , except for the density itself.

2. Calculate  $D_{\min} = D(\rho = \rho^0 X_{\min}), D_{\max} = D(\rho^0 X_{\max})$

3. Calculate

$$D_1 = D(\rho^0 \cdot (X_1 = 0.618X_{\min} + 0.382X_{\max})), \quad (1.22a)$$

$$D_2 = D(\rho^0 \cdot (X_2 = 0.382X_{\min} + 0.618X_{\max})) \quad (1.22b)$$

If  $D_1 > D_{\min}$  then error,  $X_{\min}$  should be decreased. If  $D_2 > D_{\max}$  then error,  $X_{\max}$  should be increased. Then, go to step 2, but if these values exceeded some predefined threshold, then fatal error.  $X_{\min}$  can't be decreased down to unity; there are no thermodynamical restrictions concerning  $X_{\max}$ .

4. If  $D_1 < D_2$ , then assign  $X_{\max} := X_2, D_{\max} := D_2, X_2 := X_1, D_2 := D_1$  and calculate  $(D_1, X_1)$  by formula 1.22. Otherwise, assign  $X_{\min} := X_1, D_{\min} := D_1, X_1 = X_2, D_1 := D_2$  and calculate  $(D_2, X_2)$  by formula 1.22.

5. Check the convergence criterion: if

$$|X_1 - X_2| < \epsilon_R \quad (1.23)$$

then calculate the final answer  $D(\rho = \rho^0 (X_1 + X_2)/2)$  with the final calculation of the state behind the wave. Otherwise go to step 4.

### The final state behind the wave is calculated as follows:

1. Density  $\rho = \rho^0 (X_1 + X_2)/2$ ;
2. Detonation speed:  $D = D(\rho)$
3. Other parameters (concentrations  $N_k$ , temperature  $T$  and pressure  $p$ ) are determined within the framework of the algorithm  $D(\rho)$

### Chemical equilibrium calculation under the condition of constant density and temperature.

To calculate the equilibrium state we will use the algorithm NASA CEA, published in the NASA report [5] in several forms. We need the equilibrium state calculation at the given temperature under the condition of constant density.

Under the constant density condition the Helmholtz energy of the mixture  $f(T, N_j)$  is minimized together with condition of elements conservation in chemical reactions:

$$b_q = \sum_{k=1}^{N_C} n_{qk} N_k = \sum_{k=1}^{N_C} n_{qk} N^v = b_q^0, q = 1, \dots, N_E \quad (1.24)$$

Here  $n_{qk}$  is a matrix of element compound of the mixture. Helmholtz energy is calculated as follows:

$$f(T, N_j) = \sum_{k=1}^{N_C} N_k f_k; f_k = E_k(T) - TS_k(T) + R_G T \ln \frac{N_k R_G \rho T}{p_B} \quad (1.25)$$

Lagrange multipliers  $\lambda_q$  by the number of elements are introduced and the target function is compiled:

$$F = f + \sum_{q=1}^{N_E} \lambda_q (\mathbf{b}_q - \mathbf{b}_q^0) = \sum_{k=1}^{N_C} + \sum_{q=1}^{N_E} \lambda_q \left( \sum_{k=1}^{N_C} n_{qk} N_k - \mathbf{b}_q^0 \right) \quad (1.26)$$

Varying 1.26, we obtain the following equilibrium conditions:

$$f_k + \sum_{q=1}^{N_E} \lambda_q n_{qk} = 0; \sum_{k=1}^{N_C} n_{qk} N_k - \mathbf{b}_q^0 = 0 \quad (1.27)$$

After introducing variations  $\Delta \ln N_k$ , denoting  $\pi_j = -\lambda_j / (R_G T)$ , considering the first member in a Taylor expansion and division by  $R_G T$ , we can infer equations for variations:

$$\Delta \ln N_k - \sum_{j=1}^{N_E} n_{jk} \pi_j = -\frac{f_k}{R_G T} \quad (1.28a)$$

$$\sum_{k=1}^{N_C} N_k n_{qk} \Delta \ln N_k = \mathbf{b}_q^0 - \mathbf{b}_q \quad (1.28b)$$

It is convenient to express concentration logarithm corrections from 1.28a through the Lagrange multipliers, reducing linear problem down to  $N_E$  equations:

$$\Delta \ln N_k = \sum_{j=1}^{N_E} n_{jk} \pi_j - \frac{f_k}{R_G T} \quad (1.29a)$$

$$\sum_{p=1}^{N_E} \left[ \sum_{k=1}^{N_C} N_k n_{pk} n_{qk} \right] \pi_p = \mathbf{b}_q^0 - \mathbf{b}_q + \sum_{k=1}^{N_C} \frac{N_k f_k}{R_G T} n_{qk} \quad (1.29b)$$

On each iteration we should solve problem 1.29b, then from 1.29a express concentration corrections and then multiply the previous value of this concentration on this corrections.

Equilibrium state of the mixture quite often differs from the initial one. That's why the choice of the initial approximation is crucial for the convergence of the iterative procedure (N.B.: don't mix it up with the initial state!). In paper [5] it is proposed to pick as initial approximation  $N_k = 0.1 / N_C$  (in case the temperature is given and we minimize the Helmholtz energy).

Iterations, obtained with the above method often give too big corrections to the variables. This happens generally in two cases. The first case is when at the beginning of the calculation the approximations are quite far from the equilibrium state. The second is when we are closer to the end of the calculation and the corrections for concentrations of substances which are present in small amounts are big. Next, molar concentration of each component is compared with value  $\epsilon \approx 10^{-8}$ . If

$N_k/N = \sum_j N_j > \epsilon$ , then correction  $N_k$  is limited with a value  $e^2 \approx 7.4$ . So, the control factor for these fractions is calculated as:

$$\lambda_1 = \frac{2}{\max\{|\Delta \ln N_k|\}} \quad (1.30)$$

In case  $N_k/N < \epsilon$  and also  $\Delta \ln N_k > 0$ , another restriction is introduced:

$$\lambda_2 = \min \left| \frac{-\ln N_j/N - 9.21}{\Delta \ln N_j} \right| \quad (1.31)$$

Resulting factor is defined as

$$\lambda = \min\{1, \lambda_1, \lambda_2\} \quad (1.32)$$

Consequential iterations of the method including correction factor are calculated as:

$$N_k^{j+1} = N_k^j \exp(\lambda \Delta \ln N_k) \quad (1.33)$$

Stopping criterion is following:

$$\frac{N_k}{N} |\Delta \ln N_k| < 0.5 \cdot 10^{-5} \quad (1.34a)$$

$$|b_i^0 - b_i| < 10^{-6} \cdot \max b_i^0 \text{ for } b_i^0 > 10^{-6} \quad (1.34b)$$

If the process doesn't converge in 50 iterations, then it is aborted. Usually, it takes from 8 to 20 iterations for the algorithm to converge from a random initial approximation; in most cases even less.

## Neumann peak conditions calculations.

Neumann peak is a head part of the detonation wave; on the primary strong discontinuity chemical reactions aren't initialized yet and the mixture compound remains the same as in front of the wave. The wave itself propagates with a fixed velocity  $D$ , which is obtained before the Neumann peak calculation under condition that behind the detonation complex chemical equilibrium is settled and that the reactions are intensive enough to complete before gas behind the wave flows behind the sonic line. Neumann peak calculation contains an auxiliary procedure of enthalpy imbalance calculation as a function of density in Neumann peak and the primary one eliminating this imbalance using Newton method.

### 1.2 Enthalpy imbalance calculation with enthalpy being the density function.

Let the initial conditions  $\rho^0, p^0, T^0, N_k^0$  and wave speed  $D$  be preset. Moreover, suppose density value on the Neumann peak  $\rho$  is given. From 1.16 it follows, that

$$v = \frac{\rho^0}{\rho} D \quad (1.35)$$

Substituting 1.35 into 1.16b, we can find Neumann peak pressure as a function of density :

$$p = p^0 + \rho^0 D^2 - \rho v^2 \quad (1.36)$$

Given pressure, density and initial compound, we can find gas temperature in Neumann peak as a function of density:

$$T = \frac{p}{\rho R_G \sum_k N_k^0} \quad (1.37)$$

Let's call imbalance of equation 1.16c the enthalpy imbalance; it is calculated according to 1.35 1.37 as:

$$\Delta H(\rho) = h(T, N_j^0) - h(T^0, N_j^0) + \frac{1}{2}(v^2 - D^2) \quad (1.38)$$

### 1.3 Neumann peak calculation

This calculation is performed after the Chapman-Jouguet conditions calculation; detonation speed is assumed to be known. As an initial approximation for density behind the jump we take mixture density behind the Chapman-Jouguet detonation wave. Then Newton method iterative procedure is started; on each iteration we subsequently calculate:

$$\Delta H_1 = \Delta H(\rho + \epsilon_\rho); \Delta H_0 = \Delta H(\rho); \Delta \rho = -\frac{\epsilon_\rho \Delta H_0}{\Delta H_1 - \Delta H_0}; \rho_+ = \Delta \rho \quad (1.39)$$

Here the enthalpy imbalance derivative is calculated by means of the finite difference for which the density increment  $\epsilon_\rho$  should be small enough. As a stopping criterion for 1.39 we can take for example,

$$|\Delta \rho| < \epsilon_\rho \quad (1.40)$$

Then the Neumann peak conditions should be calculated according to formulas 1.35 1.38; calculation of the enthalpy imbalance itself can then be left out (it can be calculated as an method inaccuracy measure) Details of detonation onset simulation peculiarities can be found in [11, 19, 20].

### 1.4 Test problem.

To test the algorithm we took the problem of detonation calculation in gas mixture of hydrogen, oxygen and nitrogen (oxygen-nitrogen ratio is 1:3.75, which is close to that in air). Mixture ignition was performed by means of simultaneous injection of mass and energy from the outside in a short period of time which simulates the use of a solid-state detonator; ignition parameters were picked in order to directly initiate detonation in gas mixture.

System geometry corresponds to a rectangular  $50 \times 5 \times 5$  cm parallelepiped. Walls are closed; initial mixture compound is  $[H_2] : [O_2] : [N_2] = 2 : 1 : 3.75$ . Initial pressure is  $P_{ini} = 1$  bar, initial temperature is  $T_{ini} = 300$  K.

Ignition is performed through the energy and mass supply into a spherical area with a radius  $r_{\text{ign}}$  within first  $t_{\text{ign}} = 2 \cdot 10^{-6}$  seconds from the beginning. Supplied mass equaled  $\Delta M = 0.335 \text{ mg}$ , extra energy (except for energy supplied with mass)  $\Delta Q = 134 \text{ mJ}$ . These parameters may correspond for example to a detonator such as 249.5 mkg of lead azide mixed with 85.5 mkg of nitrogen chloride [6], [7]. Chapman-Jouguet detonation parameters for such mixture are:

$$D_{\text{CJ}} = 1956.7 \text{ m/s}, P_{\text{CJ}} = 15.31 \text{ bar}$$

Pressure in Neumann peak propagating according to Zeldovitch-Neumann-Döring theory in front of the detonation wave:

$$P_{\text{NP}} = 27.11 \text{ bar}$$

## Numerical calculation conditions.

Two different shock-capturing methods were tested with the same parameters:

1. Explicit second-order in space and time method based on the MUSCL-interpolation of variables on a face at a convective flux calculation. Interpolation direction choice and pressure interpolation were performed by means of AUSMP method [13-18]. The method was implemented on a regular grid containing equal elements (rectangular parallelepipeds) connected generally in arbitrary topology. Source code was written in C. Parallel execution support was implemented using OpenMP library. Test calculation was performed on an Acer laptop (4 CPUs) for a grid and on a computer APC-1 (144 CPUs in total, 48 processors on each motherboard with shared memory) for grids  $500 \times 50 \times 50$ ,  $1000 \times 100 \times 100$ , and  $2000 \times 200 \times 200$
2. Explicit second-order in space and time scheme based on the Kurganov-Tadmor method. The method was implemented on a regular grid (rectangular parallelepipeds). Source codes were written in FORTRAN. CUDA [12] technology was utilized to deliver GPU computing. Test calculations were performed on a graphic card Nvidia Tesla k40 for grids entailing  $260 \times 26 \times 26$ ,  $500 \times 50 \times 50$ , and  $900 \times 90 \times 90$  elements.

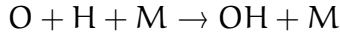
## Components list and kinetics mechanism.

Hydrogen, oxygen and nitrogen were merely the components of the initial mixture. During combustion besides the final product water vapor a manifold of intermediate products (radicals) is generated and at high enough temperature remains in the mixture. The following components were used:



In calculations we used kinetic mechanism of hydrogen combustion without nitrogen oxides formation (those reactions are reasonably slow to influence detonation and

combustion and usually are calculated a posteriori). As a basis we took Maas-Warnatz mechanism [8] which was then been developed in [9, 10]. The Kurganov-Tadmor (code 2) method used 19-step kinetics [9], while in code 3 based on MUSCL + AUSMP method additional 20<sup>th</sup> step was added taking into account one more recombination of light radicals.



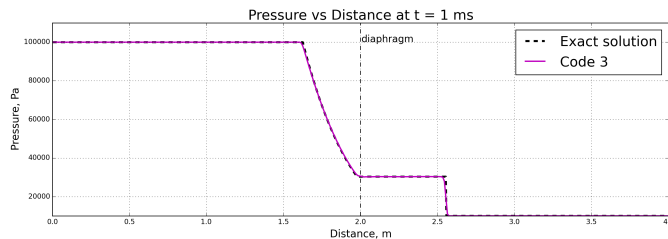
## 2 Verification of developed codes.

### Sod tests.

As a model objective for the verification of CFD solvers were picked Sod problems [21], [22], in which the result of the numerical solution of one-dimensional Riemann problem is compared with the analytical solution obtained by u-p diagrams method. A brief description of the setup is as follows: the gas is placed in the tube and divided by a partition (diaphragm). From the left of the diaphragm the state of the gas is characterized by pressure  $p_L$ , density  $\rho_L$  and speed  $u_L$ ; similarly, the options to the right of the partition are  $p_R$ ,  $\rho_R$ ,  $u_R$ . In the beginning of computation the partition is removed, and we monitor the evolution of discontinuity present in the initial data. The mixture in these tests is *nonreactive*. Two tests were conducted, the parameters of which are given in the table:

Test	$p_L$	$\rho_L$	$u_L$	$p_R$	$\rho_R$	$u_R$	T
1	$10^5 \text{ Pa}$	$1 \text{ kg/m}^3$	$0 \text{ m/s}$	$10^4 \text{ Pa}$	$0.125 \text{ kg/m}^3$	$0 \text{ m/s}$	$1 \text{ ms}$
2	$10^5 \text{ Pa}$	$1 \text{ kg/m}^3$	$237 \text{ m/s}$	$10^4 \text{ Pa}$	$0.125 \text{ kg/m}^3$	$0 \text{ m/s}$	$1 \text{ ms}$

As can be seen, the difference between two tests is that the gas from the left of the partition in first test is at rest, and in the second it moves to the right at a speed of 237m/s, resulting in transition through the speed of sound in a rarefaction wave. The reason of the choice of such parameter values is that, as indicated in the article [22], such a transonic transition causes considerable difficulties for some methods. Figure 2.1 shows the results for the first test at time instant 1ms for the first method (MUSCL interpolation + AUSMP). We provide the profiles of values of interest along the tube axis of symmetry: In 2.2 we present the same plots for



the second method (Kurganov-Tadmor).

Figure 2.1 and 2.2 show, that for the first test setup both numerical solutions match with exact one quite well. One can notice that numerical solution is good at capturing both the propagating shock wave and the contact discontinuity, which is most

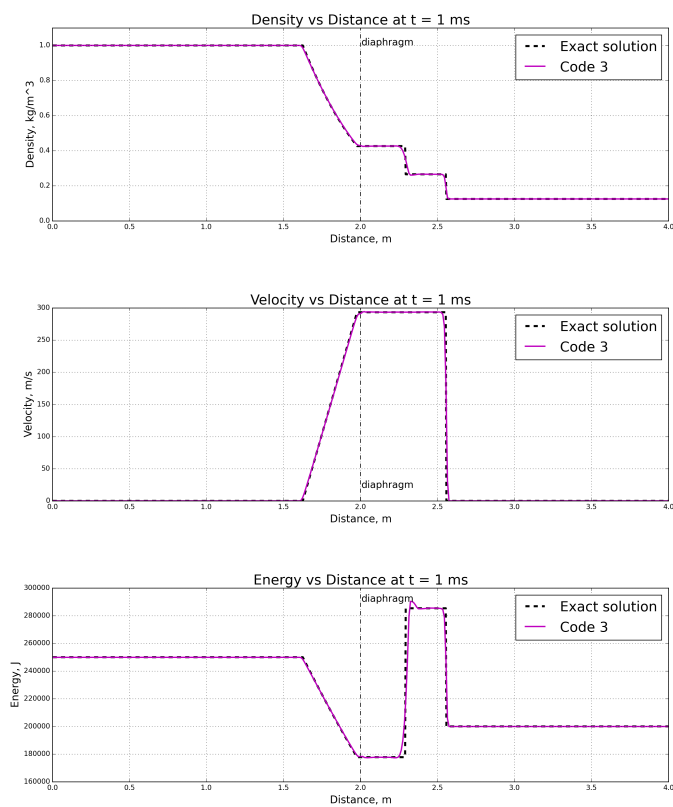


Figure 2.1: Pressure, density, velocity and energy profiles along the symmetry axis at time instant 1ms for test one for MUSCL + AUSMP method (numerical and exact solutions)

evident from the Density versus Distance plot. There is a slight oscillation on the Energy versus Distance plot for both methods though. Figures 2.3 and 2.4 present the same data for test 2:

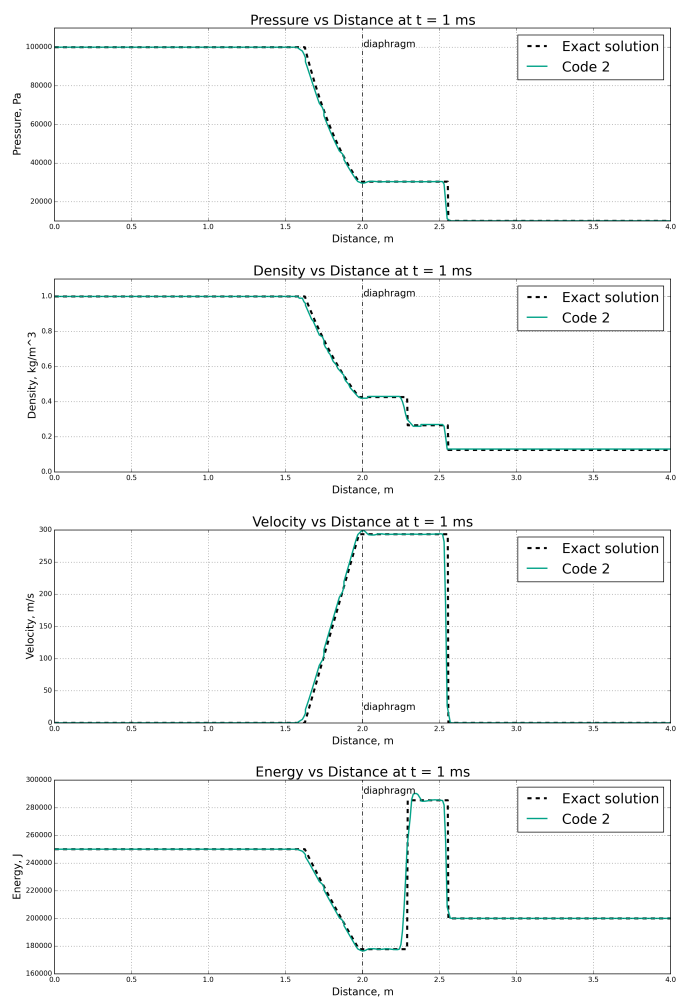
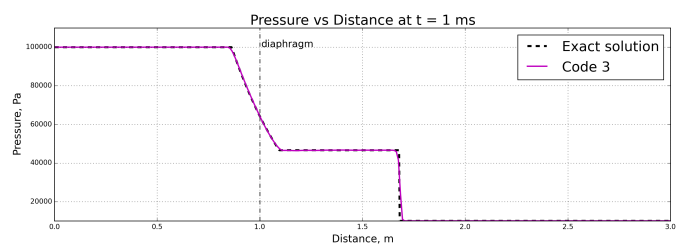


Figure 2.2: Pressure, density, velocity and energy profiles along the symmetry axis at time instant 1ms for test one for Kurganov-Tadmor method (numerical and exact solutions)



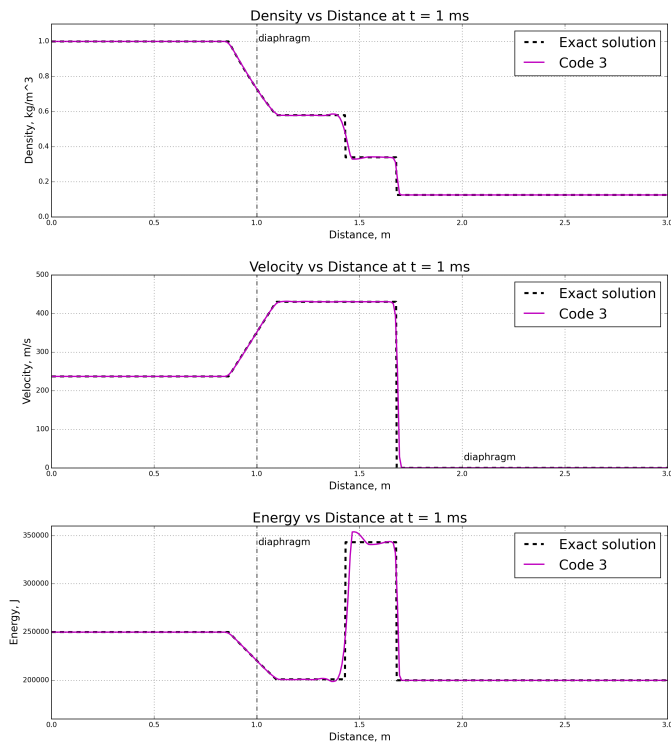
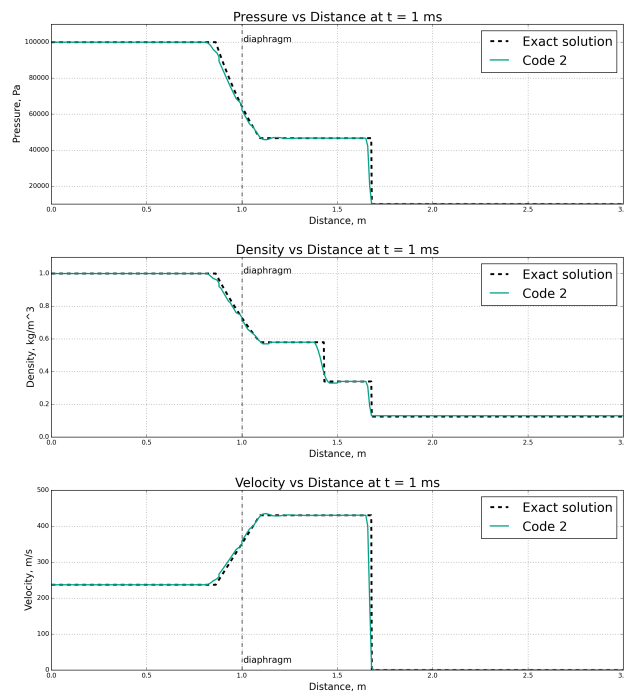


Figure 2.3: Pressure, density, velocity and energy profiles along the symmetry axis at time instant 1ms for test one for Kurganov-Tadmor method (numerical and exact solutions)



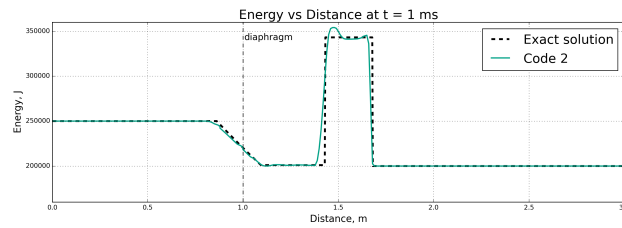


Figure 2.4: Pressure, density, velocity and energy profiles along the symmetry axis at time instant 1ms for test two for Kurganov-Tadmor method (numerical and exact solutions)

Figures 2.3 and 2.4 show, that for the second test with transonic flow in rarefaction wave (which is being washed away with counterflow and that's the reason why it stays in the diaphragm vicinity) the numerical solution still coincides well with the exact solution and transonic transition, dangerous for some methods, doesn't make these schemes collapse. On the other hand, this time the difference between the curves is more obvious and oscillations on the energy plot are a bit higher for both methods.

## Detonation initiation tests for reactive mixture.

In order to assess performance of both methods on the objectives with *reactive* fluids we considered the following setup. As in the tests above we have a tube which is separated in two halves with a diaphragm, but this time gas on the left side of the diaphragm is reactive (oxygen-hydrogen-nitrogen mixture with mass fractions  $[H_2] : [O_2] : [N_2] = 2 : 1 : 1$ ) and at low pressure (1 bar) and on the other is nonreactive ( $N_2$ ) and at high pressure (80 bar). Initial temperature in the reactive gas is 700 K and in nitrogen it is of 1500 K. Both reactive and nonreactive gases before the start of test are resting. At the beginning of calculation the diaphragm is removed and emerging shock wave, which propagates through the reactive mixture, initiates detonation. Results of this test were also compared with the exact solution obtained by u-p diagrams method.

In figure 2.5 we present profiles of main parameters at time instant 0.1 ms along the tube symmetry axis for time instant 0.1 ms and for both schemes along with the exact solution. Figure 2.5 again shows a descent coincidence between numerical solutions and the exact one. Evidently, Kurganov-Tadmor method appears to have its detonation wave propagated further, than for MUSCL-AUSMP. Most likely this is linked not with different speed of detonation propagation calculated on both methods but with the difference in the ignition delay. The intermediate product  $HO_2$  is shown to trace flame zone. Its different value at flame surface for different Codes is due to a slight difference in chemical kinetics used. The Kurganov-Tadmor (code 2) method used 19-step kinetics, while in code 3 additional 20<sup>th</sup> step was added taking into account one more recombination of light radicals. Slightly lower temperature level behind the detonation wave shown by both schemes may be due to dissociation effect, which isn't taken in account in exact solution.

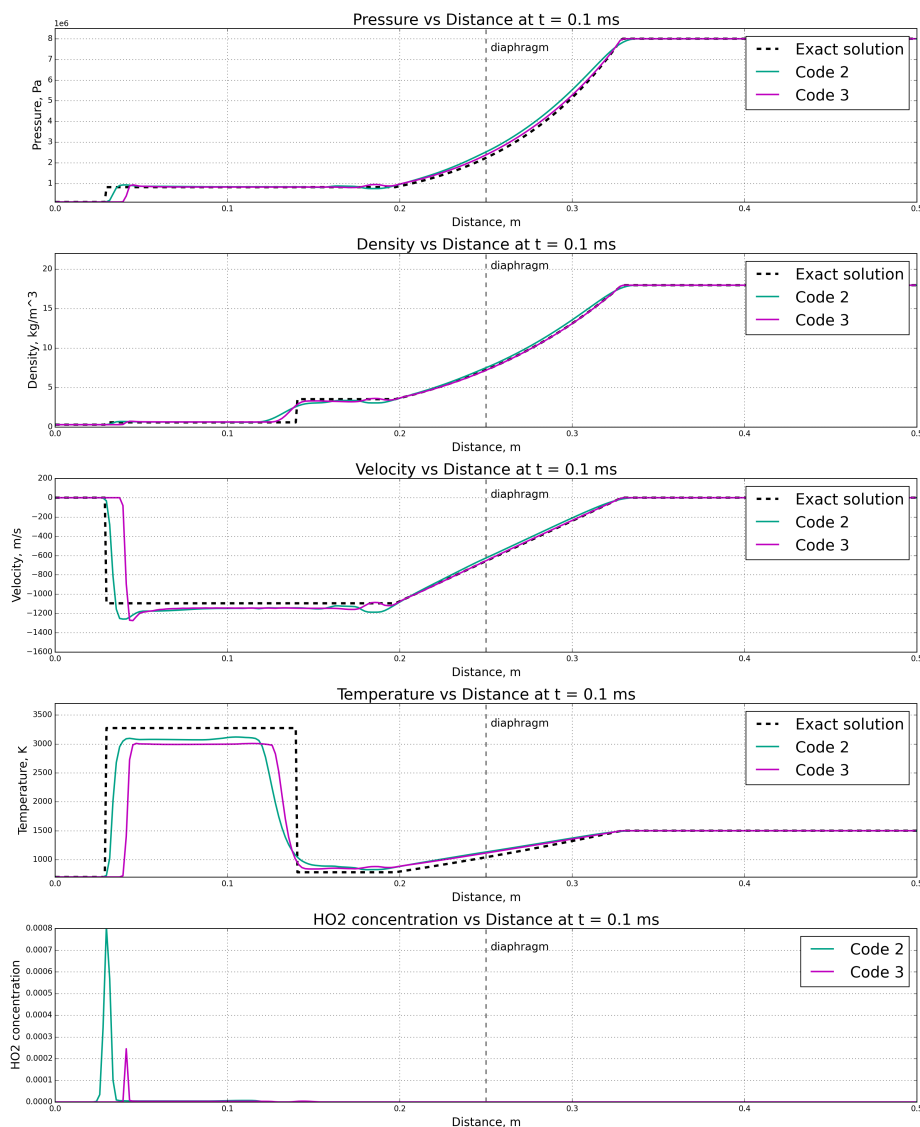


Figure 2.5: Pressure, density, velocity temperature and HO2 concentration profiles along the symmetry axis at time instant 0.1ms for test two for both MUSCL + AUSMP (code 3) and Kurganov-Tadmor (code 2) methods along with the exact solution.

### 3 Numerical simulations results and analysis.

#### Ignition tests

The computational domain was a parallelepiped sizing  $50 \times 5 \times 5$  cm. We used grids with  $260 \times 26 \times 26$ ,  $500 \times 50 \times 50$  and  $2000 \times 200 \times 200$  cells; as the data were bound to cell centers, number of nodes and number cells equaled. Grids consisted of equal cubic elements with a side size equal to 1.92, 1.0, 0.5 and 0.25 for each grid respectively. Calculations on the first (most coarse) grid were performed on Acer Aspire 5755G laptop with 4-core i7 processor. With other grids we used compact supercomputer APC-1 utilizing 144 CPUs with a peak performance of 1 Tflops. In

our simulations though we used maximum 48 processors simultaneously. On the former three grids calculation was carried out till time instant of  $250 \mu\text{s}$ , on the latter (most fine grid entailing 80 million cells) only till  $100 \mu\text{s}$ ; the reason is too long computation time even when utilizing parallelization (it takes 3 hours to calculate  $2 \mu\text{s}$  on 48 processors) and emerging from time to time bugs in performance of APC-1 slowing down computation even more. Computation on this grid was started in December 2014 (until than manifold code tests were performed) and is planned to prolong up to  $250 \mu\text{s}$  in January 2015.

Besides the main calculation on the grid  $500 \times 50 \times 50$  we've tested computation time of the first  $10 \mu\text{s}$  on a different number of processors on APC-1, from 1 up to 48; additionally we've tested code performance without using OpenMP.

Figures 3.1-3.3 show pressure in Oxy plane, passing through the symmetry axis of a computational domain. Pressure in this plane is provided for time instants 50, 100, 150, 200 and  $250 \mu\text{s}$  from the start of initiation. Lower on the figure we've depicted pressure along the symmetry axis for time instants 25, 50, 75, 100 and  $125 \mu\text{s}$ . Figure (3.1) corresponds to a  $260 \times 26 \times 26$  grid, fig. (3.2) - to  $500 \times 50 \times 50$  grid and fig. (3.3) to  $1000 \times 100 \times 100$  grid. Theoretical Chapman-Jouguet pressure levels and pressure in Neumann peak are also provided in the plot.

In fig. (3.4) pressure calculated for  $2000 \times 200 \times$  grid is shown. The difference from fig. 3.1 3.3 is that data are provided only for time instants 50 and  $100 \mu\text{s}$ ; other data have the same formats as those described above.

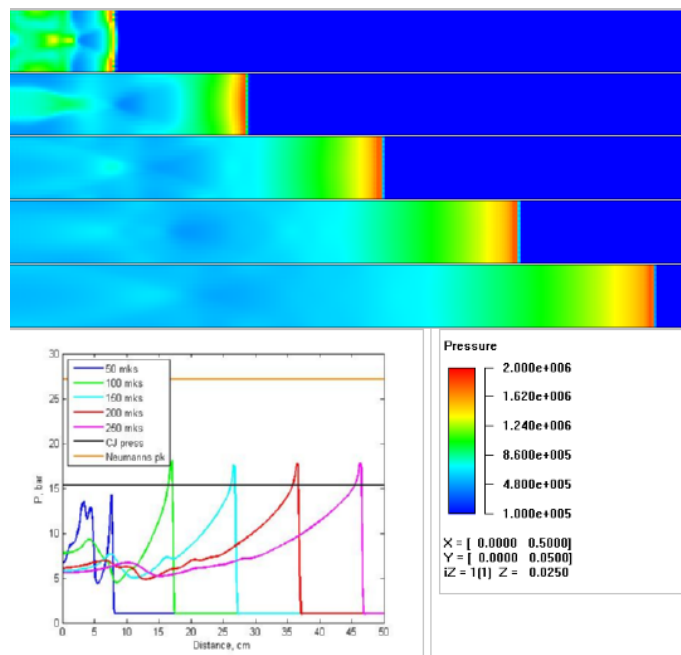


Figure 3.1: Pressure, computed on a  $260 \times 26 \times 26$  grid. Top Oxy plane section for time instants 50, 100, 150, 200 and  $250 \mu\text{s}$ . Bottom left pressure along Ox axis in the middle of the system for the same time instants, on the right colormap.

Pressure evolution pattern shows how a detonation process evolves after the initiation: there is a leading wave with a typical for detonation profile and behind it manifold secondary shock and rarefaction waves resulting from multiple wall reflec-

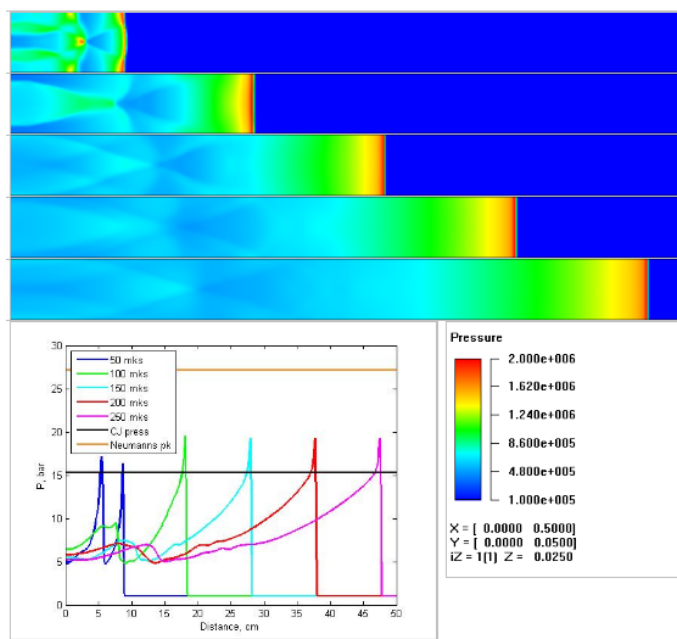


Figure 3.2: Pressure, computed on a  $500 \times 50 \times 50$  grid. Top Oxy plane section for time instants 50, 100, 150, 200 and 250  $\mu$ s. Bottom left pressure along Ox axis in the middle of the system for the same time instants, on the right colormap.

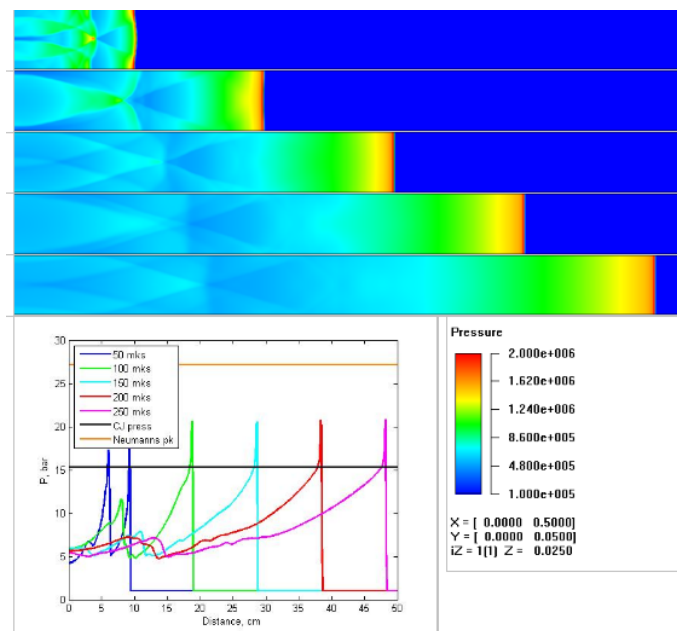


Figure 3.3: Pressure, computed on a  $1000 \times 100 \times 100$  grid. Top Oxy plane section for time instants 50, 100, 150, 200 and 250  $\mu$ s. Bottom left pressure along Ox axis in the middle of the system for the same time instants, on the right colormap.

tions. At the instant 50  $\mu$ s from the initiation pressure amplitude of a secondary wave is close to pressure value in the leading wave. With evolution of the process the secondary waves drop behind the leading wave and decrease in amplitude. On the more coarse grids both secondary wave pattern and primary detonation wave

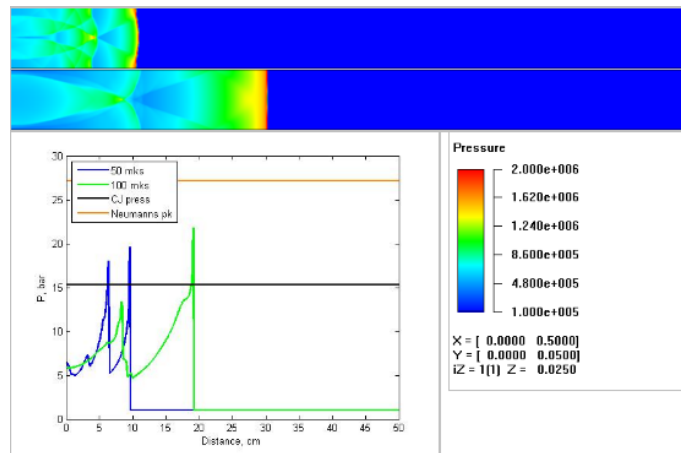


Figure 3.4: Pressure, computed on a  $2000 \times 200 \times 200$  grid. Top Oxy plane section for time instants 50 and 100  $\mu$ s. Bottom left pressure along Ox axis in the middle of the system for the same time instants, on the right colormap.

are more smeared and their maximums are smoothed. On the more fine grids more and more features of the wave pattern emerge. In addition one can see how with the increase of grid resolution the peak of the detonation wave also rises however not reaching the theoretical value of Neumann peak.

For a further description of the process we will use  $1000 \times 100 \times 100$  grid. Data on the comparison of computations on different grids will be also provided.

In fig. 3.5 the evolution of pressure field in Oxy plane is shown for instants 25, 50, 75, 100 and 125  $\mu$ s. The colormap is from the bottom of the figure.

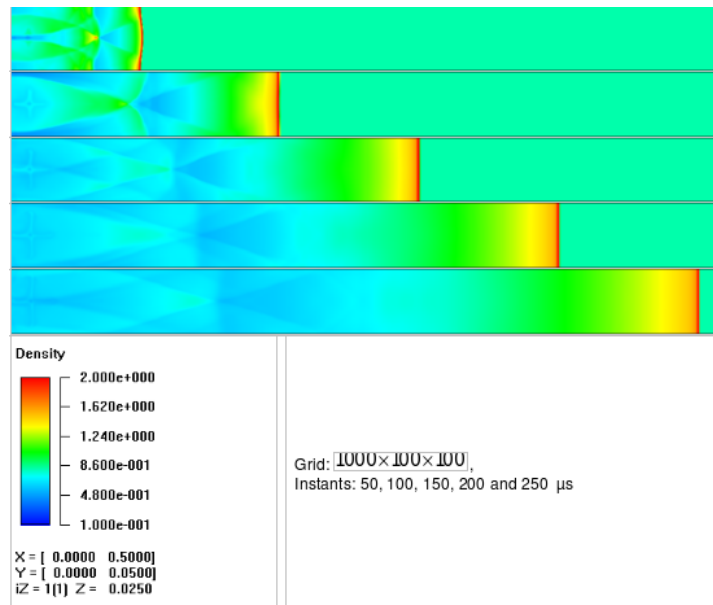


Figure 3.5: Pressure evolution in the symmetry plane of the system, Oxy.

Density pattern in general repeats that for pressure but from the left of the system one can see a cross-shaped structure - a trace of waves interaction with the primary

initiation area. The reason for such a shape of an initially round domain as will be shown further is an artifact of the numerical method. One can also observe (better than on the pressure figure) how the amplitude of far dropping behind from the leading wave focus area of the reflected shock waves decreases.

In fig. 3.6 the evolution of temperature field in Oxy plane is shown for the same time instants as for density on fig. 3.5. Colormap is from the bottom of the figure. After the detonation wave passes by, chemical equilibrium (approximately due to

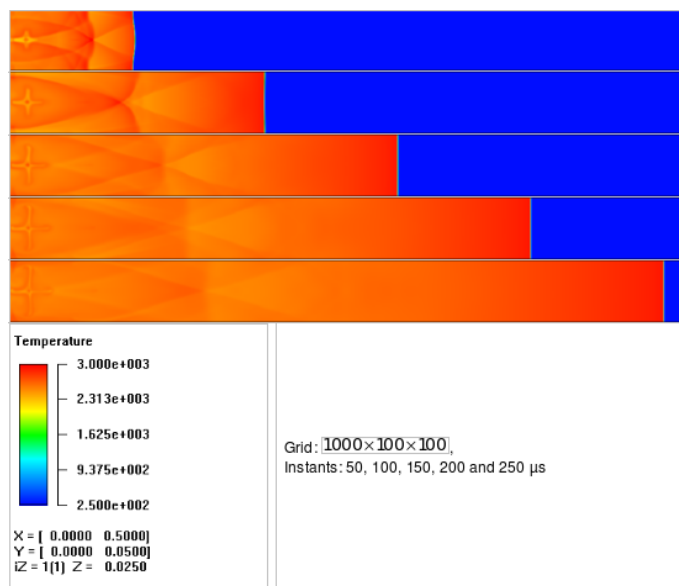


Figure 3.6: Temperature evolution in the symmetry plane of the system, Oxy.

dynamics) settles in the system. Temperature changes in the range of 2500 – 2800 K in this area highlight the wave pattern: in compression waves the temperature is increased and in the rarefaction waves decreased. One can also see the evolution of the cross-shaped structure in the area of initial influence.

On fig. 3.7 the evolution of velocity magnitude field in Oxy plane is shown for the same time instants as for density on fig. 3.5 and temperature on fig. 3.6. Colormap for the velocity magnitude is from the bottom of the figure.

Velocity magnitude pattern tracks pressure pattern (the leading wave and the rarefaction waves). One can see how after 100  $\mu$ s from the start of the process the velocity magnitude in reflected waves significantly decreases.

To better track the reflected waves, we must show the  $V_y$  component evolution in time. On fig. 3.8 the evolution of y-component of the velocity field in Oxy plane is shown for the same time instants as for fig. 3.5-3.7. Colormap is from the bottom of the figure; negative value in this case corresponds to the direction UP of y-component of velocity, and the positive one DOWN (opposite to usual representation).

Pattern for the transversal velocity component shows how the transverse waves in the system evolve and decay. Leading detonation wave location can be seen on fig. 3.8 only for instants 50 and less for 100  $\mu$ s; then detonation wave becomes almost flat and transverse velocity component gets small enough so that it can be seen at this color scale. One can also observe the decay of the transverse waves.

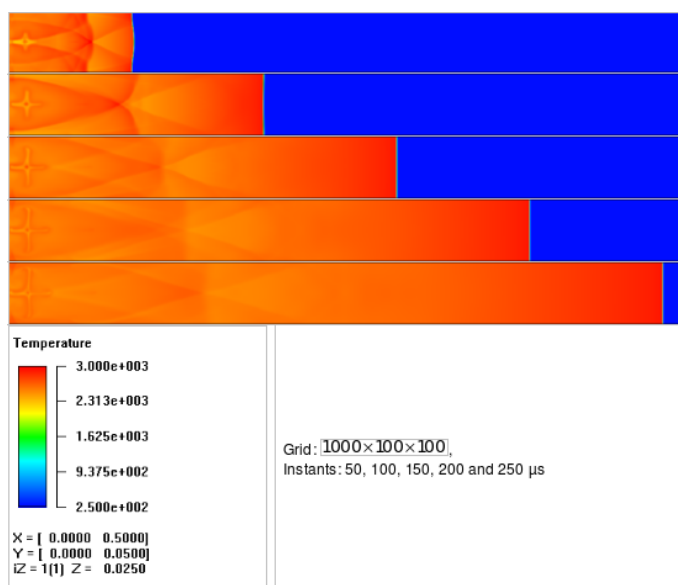


Figure 3.7: Velocity magnitude evolution in the symmetry plane of the system, Oxy.

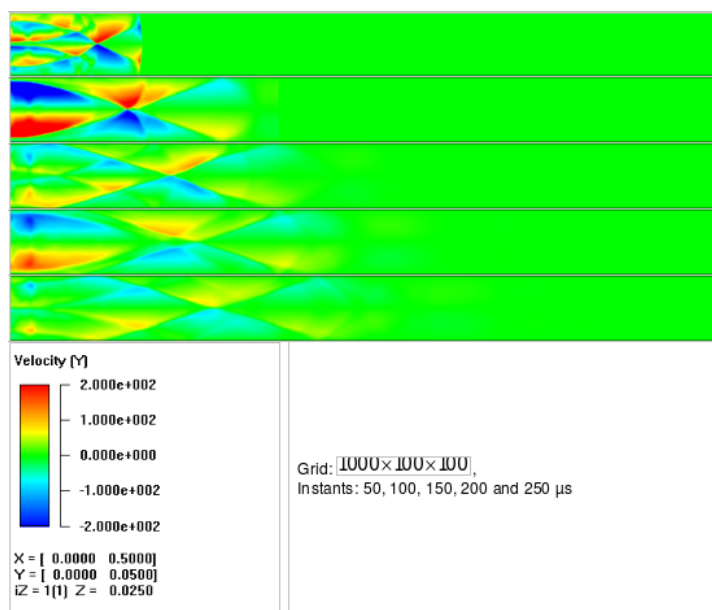


Figure 3.8: Evolution of the transversal component of velocity field in the symmetry plane of the system, Oxy.

In the utilized kinetics mechanism the crucial role is played by radical  $\text{HO}_2$  (perhydroxyl). The thing is that this component takes a critical part in primary dissociation of the initial products  $\text{H}_2$  and  $\text{O}_2$  and additionally it rapidly dissociates at high temperatures. Thus, perhydroxyl concentration fits well for the hydrogen-oxygen combustion waves tracking on the combustion wave it is of 2 orders higher than in chemical equilibrium areas. At the same time this material is present also in the chemical equilibrium domain tracking the features of wave pattern (as well as temperature, density and so on).

On fig. 3.9 the evolution of  $\text{HO}_2$  molar fraction field in Oxy plane is shown for the

same time instants as for fig. 3.5 -3.8. Colormap is from the bottom of the figure. To better resolve data with the difference of few orders we use the logarithmic scale.

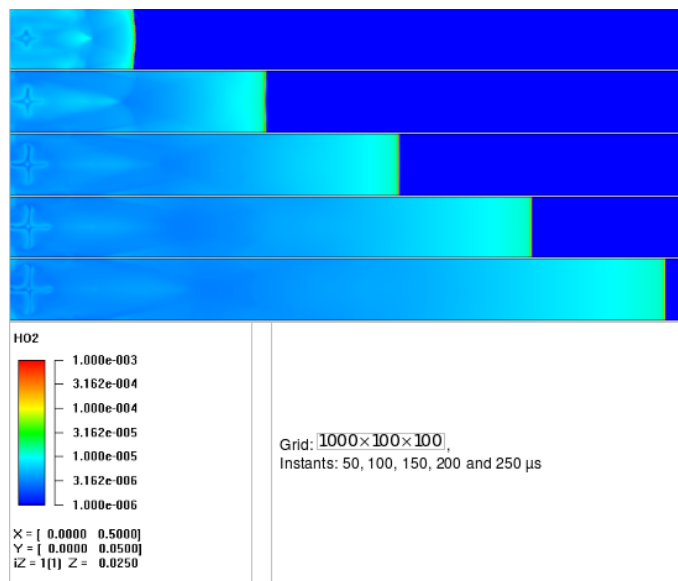


Figure 3.9: Evolution of HO<sub>2</sub> molar fraction field in the symmetry plane of the system, Oxy.

One can see, that the leading detonation wave shape in Oxy plane for instants 50 and 100  $\mu$ s isn't flat yet but later flattens. One can notice a gradual decrease of HO<sub>2</sub> concentration behind the detonation wave; it is due to that in equilibrium state it decreases with temperature decrease and the latter gradually drops behind the wave. Cross-shaped structure in place of the primal initiation is quite apparent on the figure of HO<sub>2</sub> molar fraction evolution.

Figures 3.10 - 3.13 are dedicated to comparison of pressure, temperature, magnitude of velocity and HO<sub>2</sub> molar fraction fields calculated at the instant 50  $\mu$ s, from the start of the process for different grids: 260x26x26, 500x50x50, 1000x100x100 and 2000x200x200. From figure 3.10 one can infer that as the grid resolution increases, the wave location moves right. This (as it is shown below) isn't due to the increase in wave speed but more with the increase in primal detonation initiation delay on the more coarse grids because of the numerical diffusion such a crucial for detonation initiation conditions parameters as temperature and radicals concentrations. One as well can see that for 1000x100x100 and 2000x200x200 grids this effect is already inconspicuous and the results are quite alike, though the resolution of wave processes on the more thin wall is much better (this can be seen comparing figures 3.2 and 3.3 and also will be shown below)

On the coarse grid one can also see pressure oscillations in the vicinity of the leading detonation wave, which are significantly decrease on the more fine grids (for resolution of fig. 3.10 oscillations are inconspicuous).

Temperature field in whole tracks the pressure field; on fig 3.11 it is also well seen that the cross-shaped structure in place of the primal initiation is 2 times decreased in size on 2000x200x200 in comparison with its size on the 1000x100x100 grid; on the more coarse grids this structure is blurred

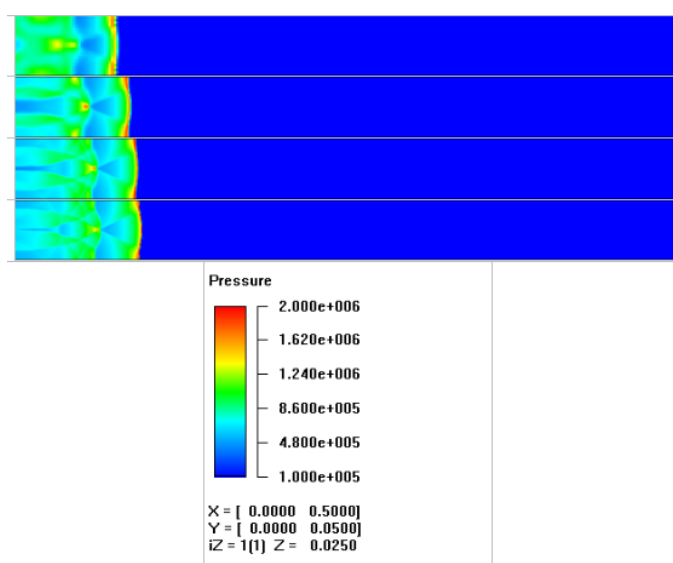


Figure 3.10: Pressure field in Oxy plane at instant  $50 \mu\text{s}$  from the beginning of the process, for grids  $260 \times 26 \times 26$ ,  $500 \times 50 \times 50$ ,  $1000 \times 100 \times 100$  and  $2000 \times 200 \times 200$

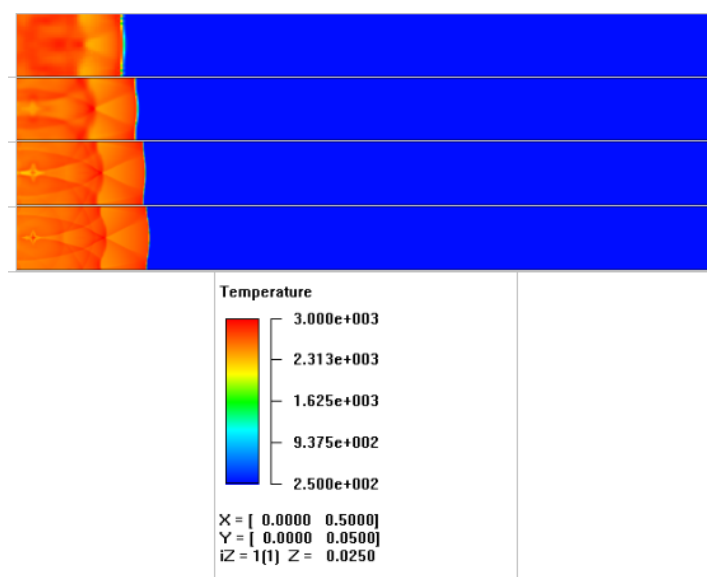


Figure 3.11: Temperature field in Oxy plane at instant  $50 \mu\text{s}$  from the beginning of the process, for grids  $260 \times 26 \times 26$ ,  $500 \times 50 \times 50$ ,  $1000 \times 100 \times 100$  and  $2000 \times 200 \times 200$

By the change in velocity magnitude field with the changing grid resolution one can clearly notice a decrease in the numerical smearing as the spatial grid step size decreases. The cross-shaped structure on the place of primal initiation the velocity field doesn't track at all, or it is inconspicuous for the colormap of fig. 3.12. Also one can see significant velocity oscillations on the coarse grid in the vicinity of the leading detonation wave, which disappear on the thin walls.

On figures for  $\text{HO}_2$  molar concentration field a different degree of smearing of the structures behind the wave as well as oscillations in vicinity of the leading detonation wave are well seen on the most coarse grid. Cross-shaped structure in place of the

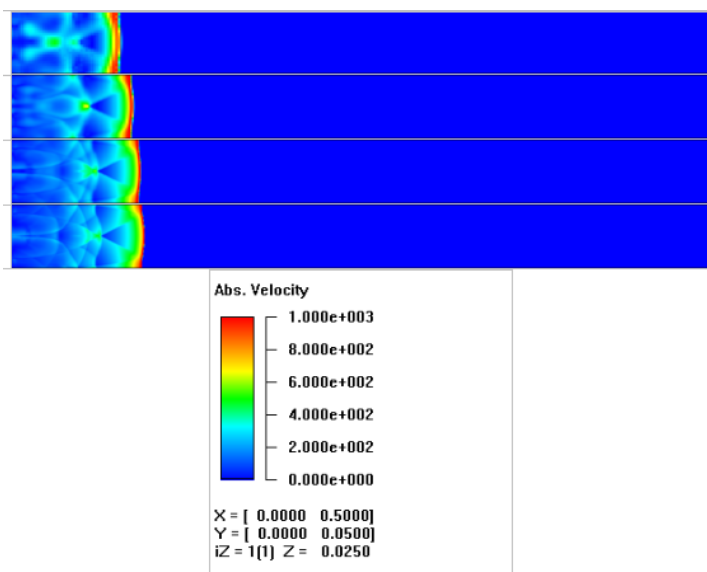


Figure 3.12: Velocity magnitude field in Oxy plane at instant  $50 \mu\text{s}$  from the beginning of the process, for grids  $260 \times 26 \times 26$ ,  $500 \times 50 \times 50$ ,  $1000 \times 100 \times 100$  and  $2000 \times 200 \times 200$

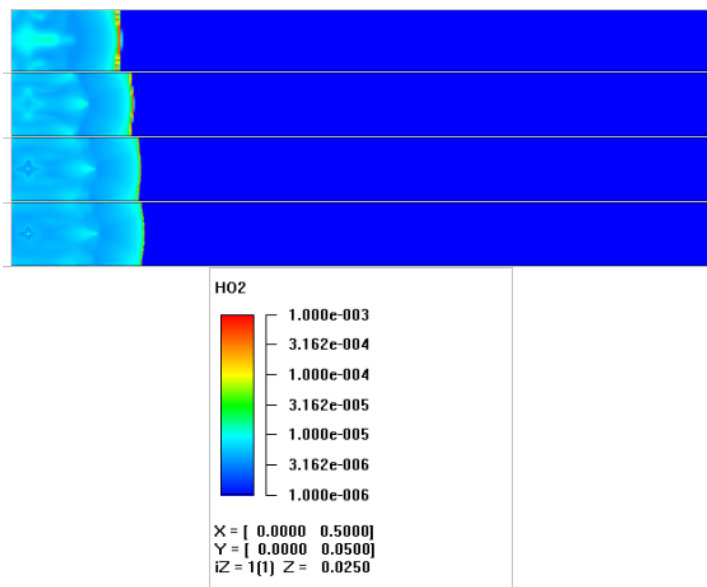


Figure 3.13:  $\text{HO}_2$  (perhydroxyl) molar fraction field in Oxy plane at instant  $50 \mu\text{s}$  from the beginning of the process, for grids  $260 \times 26 \times 26$ ,  $500 \times 50 \times 50$ ,  $1000 \times 100 \times 100$  and  $2000 \times 200 \times 200$

primal initiation is seen on all the grids, simply on the most coarse grid it is so blurred that it occupies almost the entire cross section. One can see that each time it decreases in size almost twice with the spatial step 2 times decrease and thus we can conclude that this is one of the computational effects which is diminished when resolution increases.

Thus,  $\text{HO}_2$  distribution pattern (in case we use the logarithmic scale) is one of the most informative characteristics both for the qualitative nature of the combustion

processes and for the influence of a grid size on computation.

Below, on fig. 3.14 The HO<sub>2</sub> radical concentration field is shown for the instant 100 μs for the same grid sizes as in fig. 3.13 Distribution pattern of the HO<sub>2</sub> molar

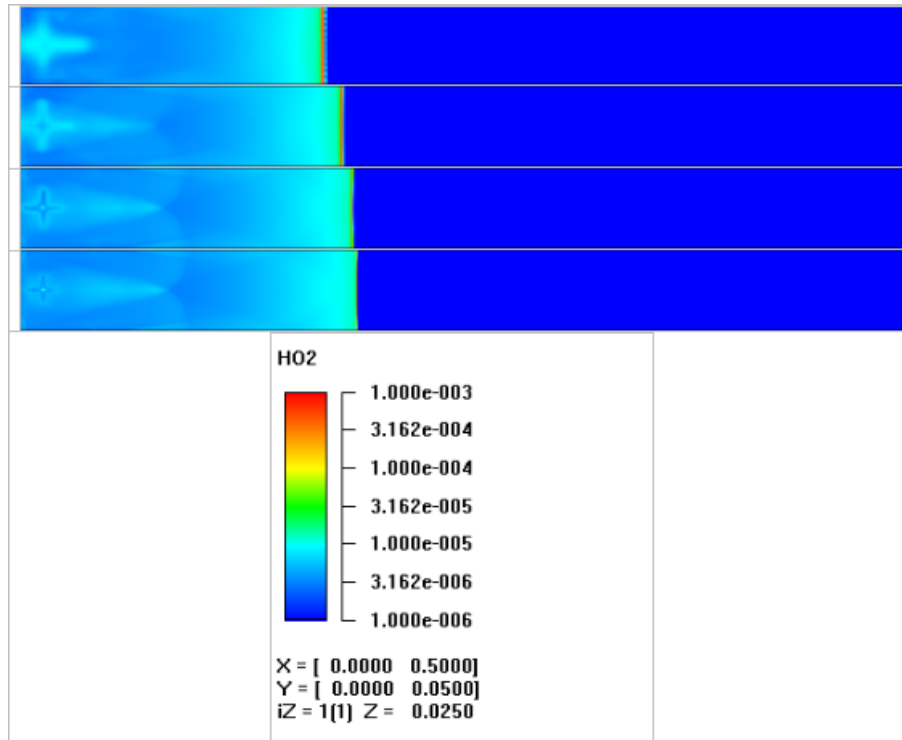


Figure 3.14: HO<sub>2</sub> (perhydroxyl) molar fraction field in Oxy plane at instant 100 μs from the beginning of the process, for grids 260×26×26, 500×50×50, 1000×100×100 and 2000 × 200 × 200

fraction at 100 μs from the start of the process confirms the conclusions which were made based on fig. with 50 μs, obtained for different grids. One can notice that the degree of smearing and the size of cross-shaped structure on the coarse grids is much more clear here than in fig. 3.13

Fig. 3.15 shows the state of mass fraction profiles for all the chemical products along the central axis of the computational domain at instant  $t = 100 \mu s$  from the beginning of the process. For concentrations the logarithmic scale is used. The figure includes data for calculations on all 4 used grids.

Fig. 3.15 shows how the initial mixture compound (from the right of the jump-like transition in vicinity of 17 – 20 cm from the left end of the system) approaches the chemical equilibrium state (from the left of transition) and how the equilibrium state changes due to temperature oscillations in the transversal waves behind the leading detonation wave and in vicinity of the primal initiation. It is seen that as system approaches the equilibrium state:

- Nitrogen concentration doesn't change (almost; its small deviations which can't be seen in this scale, happen due to different numerical diffusion of the components)

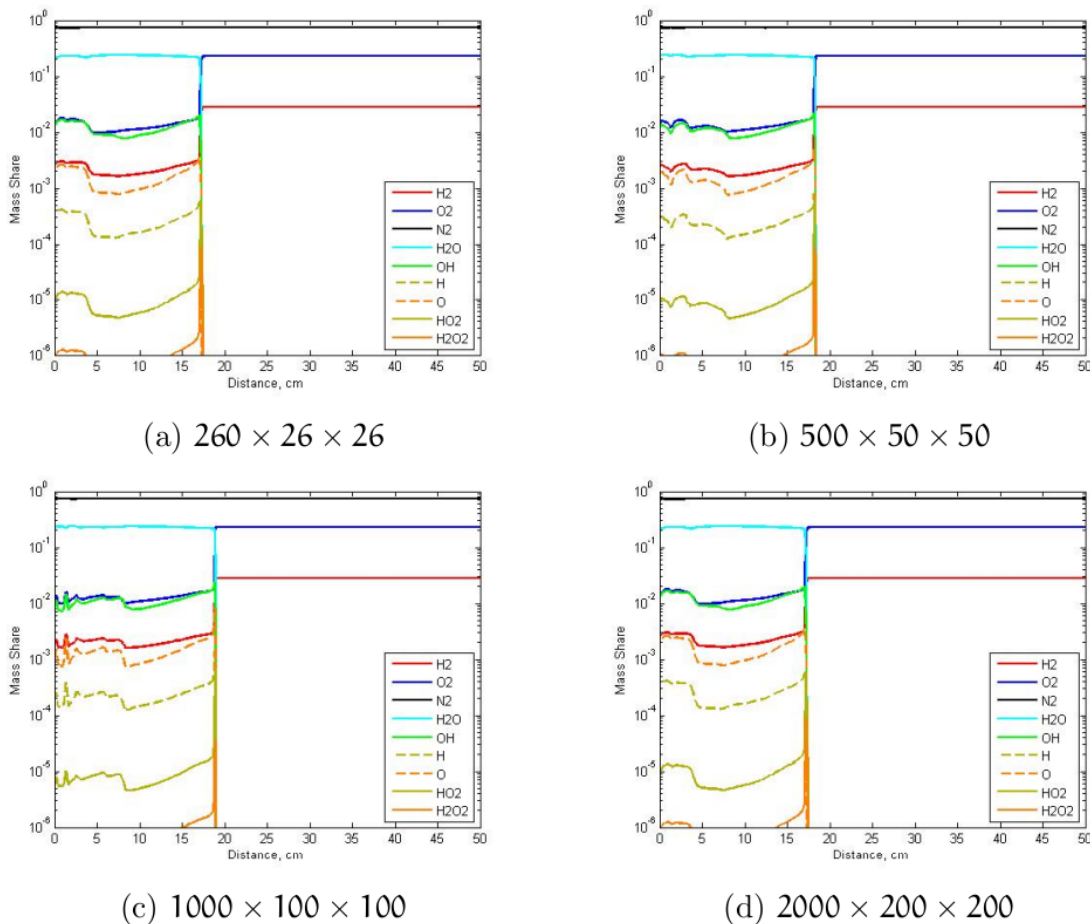


Figure 3.15: Mass fraction profiles for all the chemical components along the central axis of the computational domain at instant  $t = 100 \mu\text{s}$  from the beginning of the process.

- Oxygen concentration for a given (stoichiometric) mixture drops in combustion much less (about an order) than hydrogen concentration.
- Concentration of the light radical OH (hydroxyl) almost equals at the equilibrium state the oxygen concentration, it is the highest within all the radical concentrations, about 1%.
- Atomic oxygen concentration in the equilibrium state is of an order higher than that of the atomic hydrogen, which is most probably explained by the corresponding ratio of the molar components.
- Heavy radical  $\text{HO}_2$  concentration has a sharp maximum at the detonation wave, dropping by two orders at once and then decreasing gradually. The reason for the last drop is the pressure change behind the detonation wave; the lower the pressure the lower the concentration of this radical in the equilibrium state. In the equilibrium state it is of two orders lower than the atomic hydrogen concentration.

- $\text{H}_2\text{O}_2$  concentration mostly behaves like the  $\text{HO}_2$  concentration but of an order lower in value.

Detonation wave vicinity on fig. 3.15 is almost unresolved; on fig. 3.16 mass fractions of all the components are shown but this time in a 2 cm domain on each plot in the vicinity of the detonation wave at  $100 \mu\text{s}$  instant from the beginning of the process. As for the different grids the location of the detonation wave is somewhat shifted, on the different subplots of this figure the concentrations state is shown for the ranges from 16 to 18 cm, from 17 to 19 cm or from 18 to 20 cm.

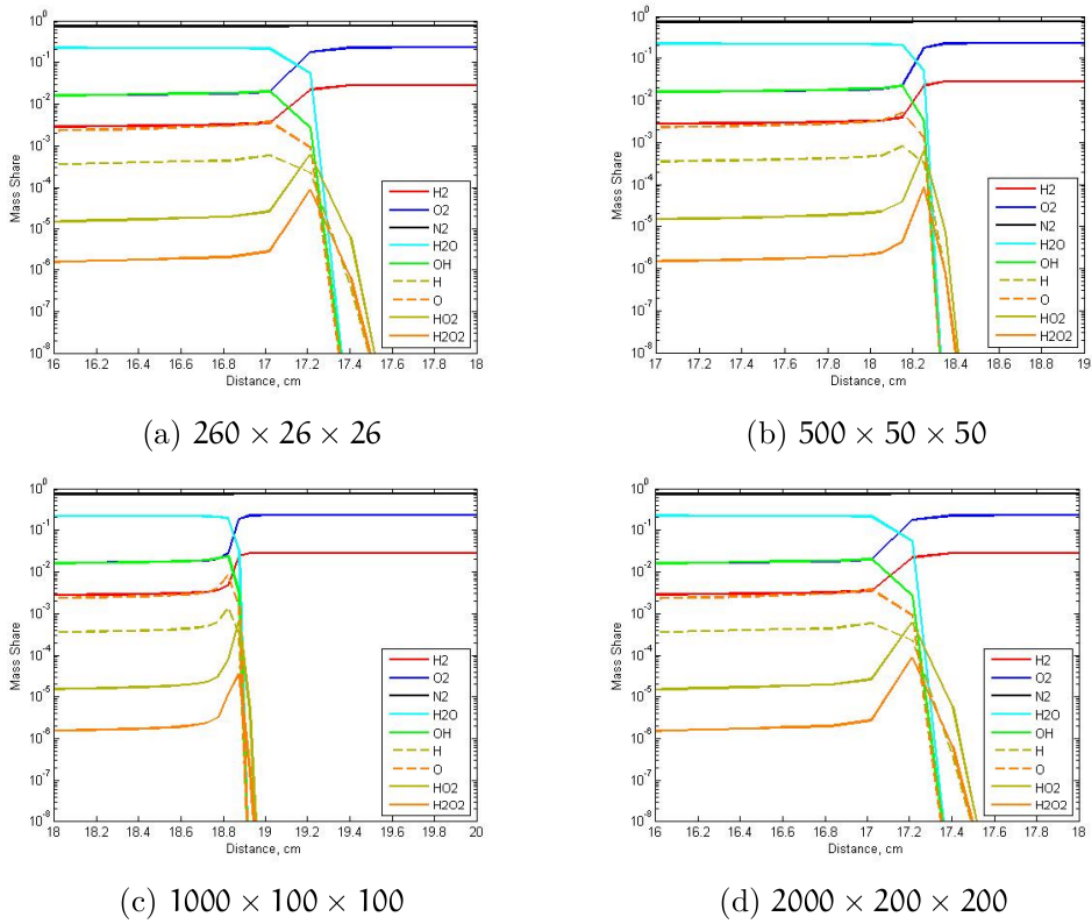


Figure 3.16: Mass fraction profiles for all the chemical components along the central axis of the computational domain at instant  $t = 100 \mu\text{s}$  from the beginning of the process in the 2 cm vicinity of detonation wave.

On fig. 3.16 one can see features of the transition area from the chemically nonequilibrium (initial) state towards the equilibrium one in the detonation wave. In the transition domain  $\text{OH}$ ,  $\text{O}$  and  $\text{H}$  radicals concentrations have a small maximum (for atomic hydrogen the exceeding compared to the equilibrium one is of a half an order, for others less) The concentration of heavy radicals,  $\text{H}_2\text{O}_2$  and  $\text{HO}_2$  has a sharp maximum of about 1.5 - 2 orders of magnitude above the equilibrium. One cell ahead of the main lifting radicals are the concentrations of  $\text{HO}_2$ ,  $\text{H}_2\text{O}_2$ , and  $\text{H}$ , which corresponds to the "launching" reaction of the kinetic mechanism,  $\text{O}_2 + \text{H}_2 = \text{HO}_2 + \text{H}$

and the interaction of the resulting radicals  $\text{HO}_2 + \text{H} + \text{M} = \text{H}_2\text{O}_2 + \text{M}$ . Reactions with these radicals are endothermic, and they do not lead directly to the rise of temperature, and thereby to forcing a weak detonation, even on the coarse mesh. With decreasing cell size the transition region narrows proportionally, this means, first, the effectiveness of suppressing numerical diffusion of components in the region of steep gradient, and secondly, that a reduction of cell size results into proportional reduction of the leading shock wave area, which is typical of shock-capturing schemes. However, the transition from  $1000 \times 100 \times 100$  grid to  $2000 \times 200 \times 200$  grid shows that the area in front of the wave has decreased in 2 times, but the area out on the equilibrium, though decreased but less. It says that there is a delay in the kinetic mechanism, i.e. physical, not numerical factor. At the same time in itself this reducing of the field after wave suggests that the chemical reaction delay factor even on the smallest of the investigated grids still is insufficient. Since the phenomenon of the fine structure of the detonation wave and the corresponding formation of the detonation cells is directly related to the operation of the delay factor of the chemical reaction, this suggests that for numerical calculation of such phenomena even better resolution is required.

The following figure. 3.17 shows the dynamics of the wave speed of detonation depending on time. The position of the detonation wave was determined by the point of maximum pressure at the peak of the detonation wave; the speed was determined by the ratio of finite differences for waves location and time, and smoothing was performed in order to compensate inaccuracies in determining the position of the peak.

It was obtained that in all cases, the wave velocity increases gradually, reaching al-

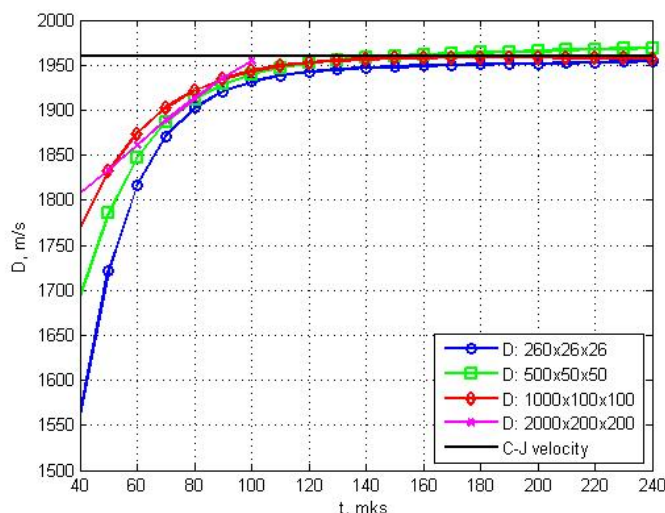


Figure 3.17: The dynamics of the detonation velocity, obtained on different computational grids

most the theoretical wave Chapman - Jouguet velocity (1956 m/s). For the coarsest mesh the final speed was slightly less for thinner a little more, for a  $1000 \times 100 \times 100$  grid practically coincided, and for a  $2000 \times 200 \times 200$  grid it has almost reached the theoretical value, but still hasn't fixed there for a time, which was calculated in the

latter case. In General, it is obtained that the lack of the wave velocity in the initial stages depends on the grid size: the finer the grid resolution, the closer speed of the wave to the theoretical. This may account for the increase in the distance traveled by the detonation wave by a fixed time instant when reducing the spatial step of the grid, visible in most of the previous drawings.

Fig. 3.18 shows the dynamics of the peak pressure in the detonation wave obtained for meshes with different resolutions. This value is shown as a function of time; control points in the figure are arranged at intervals of  $10 \mu\text{s}$ , and thus the subtle oscillations of the pressure peak the figure doesn't resolve. It was obtained that

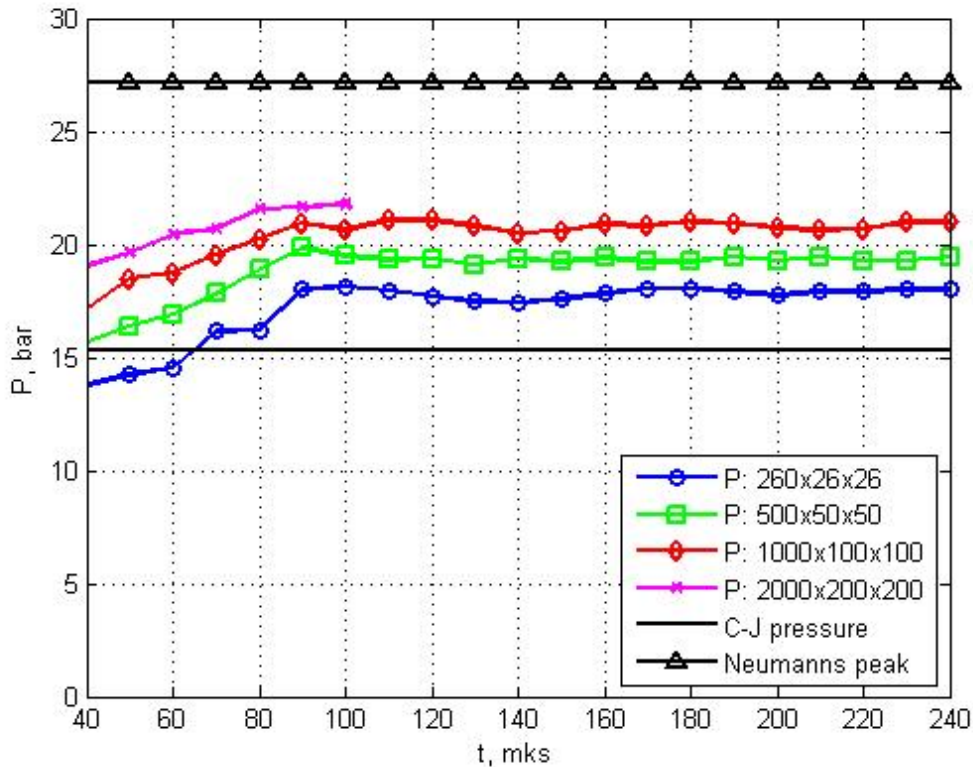


Figure 3.18: The dynamics of the peak value of the pressure in the detonation wave for meshes with different resolutions.

for time up to about  $100 \mu\text{s}$ , the peak pressure in all cases increases, then its value is stabilized. Final value is higher than the theoretical value of the pressure in the Chapman - Jouguet wave which suggests that the weak detonation due to advancing shock wave ignition of the combustible mixture of the numerical diffusion of energy or the concentration of radicals does not occur even on the coarse mesh. With the decrease of the spatial grid spacing, the peak value increases each time by about 1 bar (with decreasing step in 2 times). At the same time obtained numerically peak on these grids is by about 4 bars below the theoretical value at the Neumann peak, also marked in this figure. This assessment suggests that achieving close to Neumann peak values when using this grid should be expected with further decrease of grid step not less than for an order of magnitude. At the same time to obtain the necessary speed of detonation even the coarsest grid used is enough.

The following tests related to the performance of the method. We estimated calculation on a  $500 \times 500 \times 500$  grid for the first  $10 \mu\text{s}$  from the start of the process. The reason for choosing this grid is similar to this calculation of performance on exactly the same grid by Kurganov - Tadmor method. The performance of *MUSCL + AUSMP* method was estimated by calculation performed on personal computer APC-1Tflops utilizing 1-48 processors for the OpenMP parallelization technique and using 1 CPU without parallelization (in the graphs below that corresponds to the number "0" of processors, although certainly we used 1). A relatively long not parallelized processes, such as the output of results to file, during this calculation were disregarded, except for the final output (which, certainly, should affect performance in case the number of processors is sufficiently large).

Fig. 3.19 depicts, in logarithmic scale, the execution time of this task on APC-1Tflops for 0-48 OpenMP processes. It is seen that with increasing number of

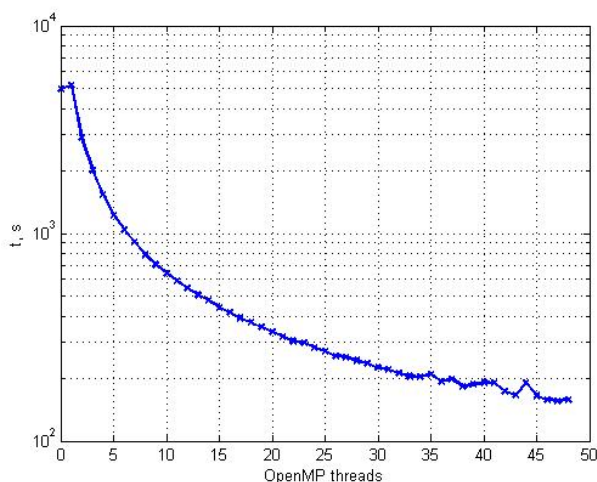


Figure 3.19: The performance on the test tasks for personal computer APC-1Tflops for various numbers of execution threads using OpenMP. Zero threads of execution corresponds to the serial code (without parallelization), one thread – the use of only one process with OpenMP enabled.

execution threads on a multiprocessor machine execution time of the task in most cases decreases. There are two exceptions: serial code (in the figure the time is shown at zero processes) is executed faster than the parallel code with one thread of execution. This is natural, since in the serial code doesn't waste computer time and other resources for the creation and maintenance of parallel processes. The second exception is the non-monotonic nature of this dependence for the number of processes above 40, i.e. close to the maximum possible number 48 for one board with shared memory. The cause for nonmonotonicity can be a transfer character, and interference of a competing system processes slowing down the calculation under the deficit of available performers.

Fig. 3.20 shows the acceleration factor, i.e. how many times the task is faster depending on the number of processes, compared with the serial code. Calculation formula is  $A(n) = T(0)/T(n)$ , where  $n$  is the number of processes,  $T$  – runtime,  $T(0)$  – serial code runtime.

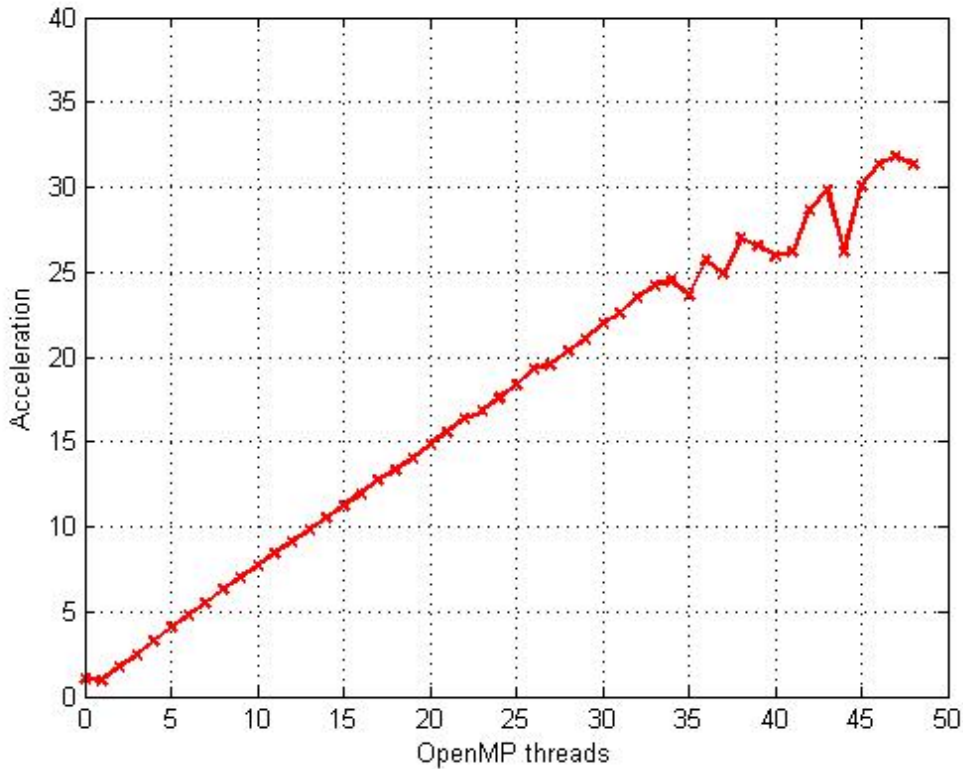


Figure 3.20: Acceleration coefficient calculation for a test task.

Fig. 3.20 shows that the acceleration up to 33 processors grows almost linearly (sagging for 1 processor), then the linearity breaks, recovering for 36 and 38 processors and approaching linear in the maximums with 43 and 47 processors. However, latter maximums should not be considered reliable enough, in the light of the observations made above in relation to execution time. However, the effectiveness (or CPU load) is less than 1, since the slope of the straight section of the acceleration is less than unity.

A graph of the efficiency of processor utilization is depicted in Fig. 3.21. The formula for calculating efficiency is  $E(n) = A(n)/n$ , and  $E(0) = 1$ . Fig. 3.21 shows that the efficiency of the first 6 processors rapidly decreases from 1 to 0.8, then slowly drops to about 0.73, up to 33 processors, almost stabilizing. Then the behavior of this characteristic becomes unstable, although the spikes are not obtained: it changes in the range 0.6–0.7. Ultimately above 33 processors, the efficiency is reduced, but still remains approximately 0.65 for the maximum (one board with shared memory) number of processors 48.

## Conclusions

- Two codes for parallel computing of detonation onset and propagation in 3-D geometry in hydrogen–air mixtures were developed and verified: one code for supercomputer based on universal processors, the other for supercomputer

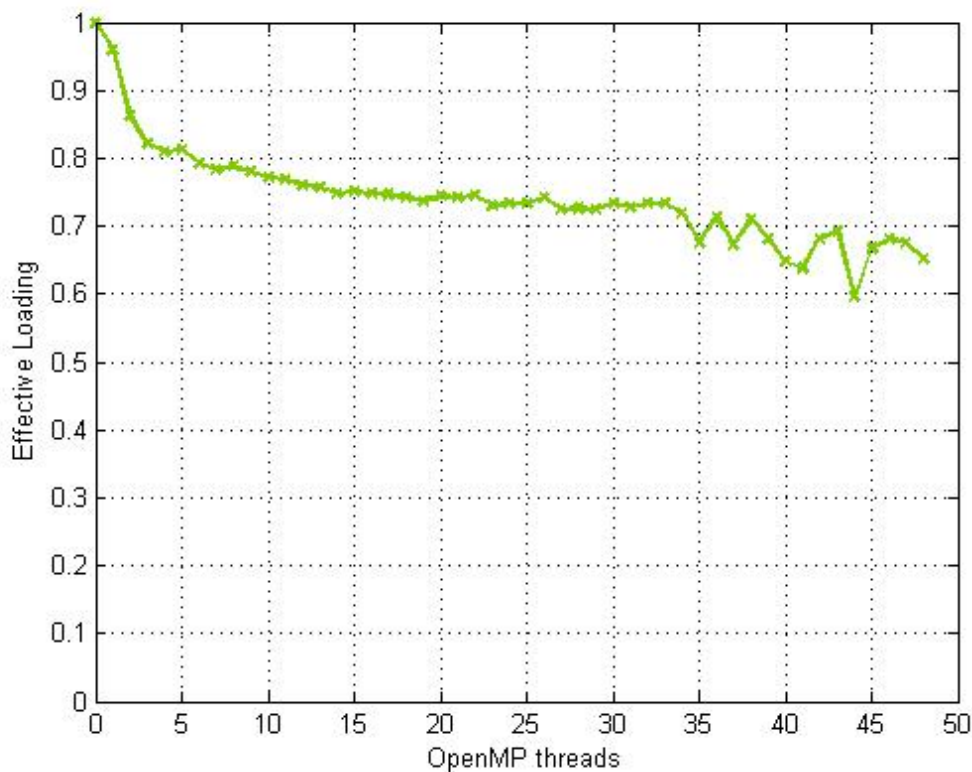


Figure 3.21: The efficiency of acceleration, or the CPUs load coefficient, as a function of their numbers when solving test problems using OpenMP.

incorporating GPGPU.

- Results of testing showed that weak detonation, due to the numerical diffusion of the  $\text{HO}_2$  radical ahead of the leading shock wave, doesn't appear even on the coarsest mesh. Although small numerical diffusion of parameters of the leading shock wave is observed.
- Numerical diffusion of parameters in front of the leading detonation wave penetrates more than 2 cells ahead of it for any investigated grid size. The maximal forward penetration is observed for the concentration of atomic hydrogen and the radicals  $\text{HO}_2$  and  $\text{H}_2\text{O}_2$ .
- With decreasing cell size the more specific features of wave patterns behind the detonation wave emerge. On coarse grids with 1250 thousand and especially 175 thousand cells many of the details are blurred by the numerical diffusion
- With decreasing cell size the detonation wave for the same time instant turns out to be further; this is especially for coarse meshes. The reason is the lower wave propagation speed before approaching ChapmanJouguet velocity; this effect is particularly noticeable for the coarse mesh and decreases with decreasing spatial step, indicating that it is of a numerical origin.

- Cross-shaped deformation under the action of shock waves in the area of primary mass and energy input is reduced in size in 2 times with decreasing cell size in 2 times. It testifies the numerical origin of the effect. Possibly the effect is associated with used in the calculation 13-point pattern having protrusions of 2 cells along each of the coordinate lines.
- The use of OpenMP technology allows to achieve almost linear acceleration of explicit methods; the deviation from linearity when the number of threads of execution on personal computer APC-1Tflops is more than 33 can be explained rather by the influence of internal data exchange processes in this computer performance than the internal weakness of the developed code. The test runs on APC-5Tflops demonstrated better results. It was obtained that the computer APC-1 allows for the calculation of multicomponent gas dynamics on a 80 million cells grid. The calculation implying several thousand time steps using parallel programming on such grid takes several days.

## References

- [1] CHEMKIN. A software package for the analysis of gas-phase chemical and plasma kinetics. CHE-036-1. Chemkin collection release 3.6. Reaction Design, September 2000.
- [2] Marinov, N.M., Pitz, W.J., Westbrook, C.K., Hori, M., and Matsunaga, N. An Experimental and Kinetic Calculation of the Promotion Effect of Hydrocarbons on the NO-NO<sub>2</sub> Conversion in a Flow Reactor. Proceedings of the Combustion Institute, Volume 27, pp. 389-396, 1998. (UCRL-JC-129372). UCRL-WEB-204236.
- [3] R.J. Kee, J.A. Miller, and T.H. Jefferson. Chemkin: a general-purpose, problem-independent, transportable Fortran chemical kinetics code package. Sandia National Laboratories Report SAND80-8003 (1980).
- [4] S. Browne, J. Ziegler, and J. E. Shepherd. Numerical Solution Methods for Shock and Detonation Jump Conditions. GALCIT Report FM2006.006 July 2004-Revised August 29, 2008.
- [5] S. Gordon, and B.J. McBride. Computer Program for Calculation of Complex Chemical Equilibrium Compositions and Applications I. Analysis. NASA RP-1311, October 1994.
- [6] Z. G. Pozdnyakov, Rossi B. D. Handbook of industrial explosives and means of blasting. M.: Nedra, 1977.
- [7] Orlova, E. J. Chemistry and technology of high explosives. Textbook for universities. Ed. 3-e, Rev. L.: "Chemistry", Leningrad branch, 1981. 312 p.
- [8] Maas, U., and Warnatz, J. Ignition process in hydrogen-oxygen mixtures. Combustion and Flame, 74, No. 1, 1988, pp. 53-69.

- [9] N.N. Smirnov, V.F. Nikitin. Modeling and simulation of hydrogen combustion in engines. *International Journal of Hydrogen Energy*. (2014), vol. 39, Iss. 2, 1122-1136. <http://dx.doi.org/10.1016/j.ijhydene.2013.10.097>
- [10] N.N.Smirnov , V.B.Betelin, R.M.Shagaliev, V.F.Nikitin, I.M.Belyakov, Yu.N.Deryuguin, S.V.Aksenov, D.A.Korchazhkin. Hydrogen fuel rocket engines simulation using LOGOS code. *International Journal of Hydrogen Energy*. (2014), vol. 39, 10748-10756.
- [11] Smirnov N.N., Betelin V.B., Nikitin V.F., Phylippov Yu.G., Jaye Koo. Detonation engine fed by acetyleneoxygen mixture, *Acta Astronautica* (2014), vol. 104, 134-146. <http://dx.doi.org/10.1016/j.actaastro.2014.07.019i>
- [12] NVIDIA CUDA. Programming Guide. 2014, <http://developer.nvidia.com/cuda-downloads>.
- [13] J.T. Ferziger, M. Peric. *Computational Methods for Fluid Dynamics*. 3d Edition, Springer, 2002.
- [14] van Leer, B. (1979). Towards the Ultimate Conservative Difference Scheme. A Second Order Sequel to Godunov's Method, *J. Com. Phys.*, 32, 101136.
- [15] Liou, M.-S., A Sequel to AUSM: AUSM+. *J. Comput. Phys.*, Vol. 129, 364-382, 1996.
- [16] Fletcher, K. *Computational methods in fluid dynamics*. In 2 volumes. TRANS. eng., Wiley, New York, 1991.
- [17] E. A. Novikov L-stable (4,2)-method of fourth order to solve hard problems. *Vestnik SamGU natural Science series*. 2011B 8(89). p. 59-68.
- [18] Koren, B. (1993). A robust upwind discretisation method for advection, diffusion and source terms. In Vreugdenhil, C.B.; Koren, B., *Numerical Methods for Advection Diffusion Problems*, Braunschweig: Vieweg, p. 117, ISBN 3-528-07645-3
- [19] N. N. Smirnov, V. F. Nikitin, S. Alari Shurehdely. Transient regimes of wave propagation in metastable systems. *Physics of combustion and explosion*, 44, 5 (2008), p. 25-37.
- [20] N.N. Smirnov, V.F. Nikitin, Yu.G. Phylippov. Deflagration to detonation transition in gases in tubes with cavities. *Journal of Engineering Physics and Thermophysics*, 83, 6 (2010), pp. 1287-1316.
- [21] Sod, G. A. (1978). "A Survey of Several Finite Difference Methods for Systems of Nonlinear Hyperbolic Conservation Laws". *J. Comput. Phys.* 27: 131. Bibcode:1978JCoPh..27....1S. doi:10.1016/0021-9991(78)90023-2.
- [22] Richard Liska, Burton Wendroff, Comparison of several difference schemes on 1d and 2d test problems for the euler equations, *SIAM J. S CI. COMPUT* . Vol. 25, No. 3, pp. 9951017

Nikitin V.F., Faculty of Mechanics and Mathematics, Moscow Lomonosov State University, Moscow 119992, Russia,

LLC "Center for Numerical Modeling", Moscow, Zelenograd 124482, Russia

Smirnov N.N., Faculty of Mechanics and Mathematics, Moscow Lomonosov State University, Moscow 119992, Russia,

Scientific Research Institute for System Studies of Russian Academy of Sciences, Moscow 117218, Russia,

LLC "Center for Numerical Modeling", Moscow, Zelenograd 124482, Russia

Stamov L.I., Faculty of Mechanics and Mathematics, Moscow Lomonosov State University, Moscow 119992, Russia,

Scientific Research Institute for System Studies of Russian Academy of Sciences, Moscow 117218, Russia,

LLC "Center for Numerical Modeling", Moscow, Zelenograd 124482, Russia

Altoukhov D.I., Faculty of Mechanics and Mathematics, Moscow Lomonosov State University, Moscow 119992, Russia